Data Driven Constitutive Model Discovery from In Silico Myocardial Biaxial Stretch Tests

by

R.P. Krijnen

EMBARGO: this thesis is under embargo until 26-11-2025

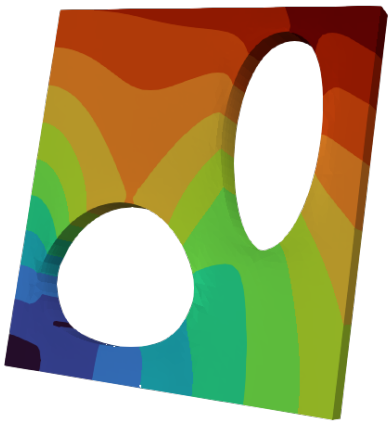

to obtain the degree of Master of Science in Biomedical Engineering
at the Delft University of Technology,
to be defended publicly on Monday December 4, 2023.

Student number:	4966937	
Master program:	Biomedical Engineering	
Graduation committee:	Dr. ir. M.P. Peirlinck	TU Delft
	Dr. S. Kumar	TU Delft
	Dr. ir. F.J.H. Gijsen	TU Delft
	Dr. A. Joshi	University of Cambridge

Data Driven Constitutive Model Discovery from In Silico Myocardial Biaxial Stretch Tests

R.P. Krijnen*

*dept. BioMechanical Engineering, Faculty of Mechanical, Maritime and Materials Engineering, Delft University of Technology

This thesis investigates the ability of Bayesian EUCLID to retrieve a predictive approximate material model for the myocardium in the presence of heterogeneous deformation fields due to simulated biaxial stretch tests. The Holzapfel-Ogden material model is used as the ground-truth material model of the simulation, since it is capable of describing the orthotropic and hyperelastic behavior of the myocardium. In total, four material models were retrieved from Bayesian-EUCLID by considering two fiber orientations within the sample and two displacement measurement techniques. The two fiber directions included one in which the sheet-like structure of the sample lies within the test plane and one in which it lies perpendicular to the test plane. The displacement field measurements considered were a full displacement field measurement and an approximation thereof based on a stereo digital image correlation method. The results show that when the sheet-like structure of the myocardium lies within the test plane of the biaxial stretch test and the full displacement field is available, Bayesian EUCLID is capable of finding orthotropic and hyperelastic material models that correspond well to the ground truth. This shows that a biaxial stretch test can adequately characterize the material behavior of the myocardium.

data-driven modeling | constitutive modeling | myocardium | biaxial test | hyperelasticity | heterogeneous deformation | fiber orientation

Correspondence: ***r.p.krijnen@student.tudelft.nl***
Supervisor: dr. ir. Mathias Peirlinck

1. Introduction

As the main driving force behind the pumping of blood throughout the body, the ventricles play a vital role in cardiac function. Ventricular tissue is divided into three parts: The epicardium, the myocardium, and the endocardium. The myocardium constitutes the bulk of the tissue and is highly influential in the mechanical behavior of the ventricles. The tissue is made up of a stacked sheet-like structure. These sheets contain two fibers: myofibers and endomysial collagen. The intricate and fibrous nature of the myocardium facilitates that the type and direction of deformation is influential in the observed mechanical behavior of the tissue, especially when sheared. This behavior differs over three mutually orthogonal axes; therefore, it is considered orthotropic. Pathological processes can lead to changes in this tissue that affect its mechanical properties. Hence, determining the mechanical properties of the myocardium is beneficial in determining both healthy and pathological cardiac function (1–3).

Mathematical models describing mechanical behavior provide a way to quantitatively argue about the behavior and the mechanical properties of the tissue. Such models are called constitutive models. In addition to formulating constitutive models based on measured behavior, they are also formulated with a priori knowledge of the constituents of the material. Several constitutitve models have been formulated in the past to capture the complex mechanical behavior of the myocardium (4–8). Some of these focus their efforts on capturing hyperelastic behavior, signifying that the energy stored within the material as a result of deformation is ever increasing. Recently, researchers have started to include viscoelastic and history-dependent effects in their models. Viscoelastic behavior includes a dependence on the rate at which the material is deformed, and thus, accounts for stress-relaxation behavior. History-dependent models can account for tissue damage due to testing. Out of the currently available models, the Holzapfel-Ogden model (HO-model) has become the de facto standard for modeling the orthotropic and hyperelastic behavior of the myocardium (9, 10). Moreover, some viscoelastic models use it as a basis for the orthotropic and hyperelastic behavior of the myocardium (6, 7). This progression of complexity in material behavior is facilitated by increasingly advanced testing procedures capable of measuring more detailed behavior.

The behavior of the myocardium is measured during mechanical tests performed on excised samples of myocardial tissue. Such measurements include the measurement of the displacement field and the forces acting on the boundary. The current method of characterizing the myocardium is laborious and requires both biaxial stretch and triaxial shear tests to capture the orthotropic behavior of the material (11, 12). In some cases, more advanced testing devices are used to reduce the number of tests and samples needed for characterization (13). This is especially beneficial for samples that are difficult to obtain, such as those taken from the myocardium.
Despite the use of sophisticated testing techniques, such as those proposed by Dokos, Sommer, and Avazmohammadi (11–13),

it is still difficult to compare results of different tests and samples due to the extensive preparation process required, which can involve the use of glue (14). When glue penetrates the material, it can affect the mechanical behavior of the sample (11).
It is also essential to consider the microstructural differences between samples, particularly when dealing with biological tissue. Additionally, the choice of measurement techniques can have an effect on the observable behavior. For example, stereo digital image correlation (SDIC) can measure the three-dimensional displacement of the top surface but cannot measure the displacement throughout the entire sample. The full displacement field can be obtained using advanced techniques such as magnetic resonance imaging (MRI) (15). As mentioned earlier, in addition to the displacement field, force measurements are also obtained. Usually, a single sensor is used per deformed boundary of the sample. Rather than measuring the variation of the forces at the boundary only a summed total is obtained.

Armed with displacement and force measurements, as well as a constitutive model, parameter fitting techniques are used to fit values to the parameters in the constitutive models. Since displacement and force data are difficult to directly correlate, traditional approaches use certain assumptions to facilitate the parameter fitting process. One of these assumptions is that the deformation throughout the material is homogeneous. This leads to measures of stress and strain, as well as a predictable deformation path, which are correlated more conveniently through the use of constitutive models. Consequently, parameter values can be found using classic parameter fitting methods. It is important to note that (naturally occurring) heterogeneous effects from the distribution of the material and the geometry are neglected or considered noise in the data (10, 14, 16).

Recently, more interest has been shown in the use of machine learning methods in the identification process of constitutive material models (17–22). The advantage of these techniques is that they can infer constitutive equations from their respective data sets, even when there are heterogeneous effects present. This eliminates the need to impose a material model in advance. Moreover, the assumption of homogeneous deformations becomes superfluous for the inference of mechanical behavior. However, it is imperative that the resulting models are physically feasible. This is achieved through implementing physical constraints in the cost functions of neural networks and/or by designing the feature-set to intrinsically satisfy these constraints.
One of these data-driven approaches, called Bayesian-EUCLID, is distinctive among the available options, as it offers statistical inference on the retrieved models and is able to produce parsimonious models from displacement and force measurements directly. This machine learning method intrinsically satisfies the constraint for physically feasible materials. This combination of parsimonious, statistically relevant, and physically feasible models aids in inferring the mechanical properties of the tested material.

Models and testing methods have become increasingly complex while still maintaining the assumption of homogeneous deformations. Naturally occurring heterogeneous deformations could be exploited during constitutive model discovery aided by machine learning. Using such methods, perhaps more complex material models can be characterized from biaxial stretch tests than previously thought. In this exploratory study, the ability of Bayesian-EUCLID to characterize orthotropic and hyperelastic materials from biaxial test measurements alone is investigated.
With reference to the previous, I hypothesize that the inclusion of heterogeneous deformations and the three-dimensional displacement field data from a biaxial stretch test allow the Bayesian-EUCLID method to discover orthotropic and hyperelastic constitutive models for the myocardium. In the current study, the Bayesian-EUCLID approach is extended and applied to heterogeneous deformation data obtained from simulated biaxial stretch tests of myocardial tissue. In total four data-sets are generated by considering two distinct fiber orientations within the sample and two displacement measurement techniques. These data sets are used as training data for Bayesian-EUCLID which yield four material models. The resulting four material models are validated against a ground truth material model, in order to assess the performance of the method.

2. Methods

2.A. Kinematics. First, I define $\boldsymbol{F}$ as the deformation gradient tensor. This tensor defines various deformation modes such as uniaxial tension (UT), biaxial tension (BT), simple and pure shear (SS, PS);

$$\boldsymbol{F}^{UT} = \begin{bmatrix} 1+\gamma & 0 & 0 \\ 0 & 1 & 0 \\ 0 & 0 & 1 \end{bmatrix} \quad \textbf{(1)} \qquad \boldsymbol{F}^{BT} = \begin{bmatrix} 1+\gamma & 0 & 0 \\ 0 & 1+\gamma & 0 \\ 0 & 0 & 1 \end{bmatrix} \quad \textbf{(2)}$$

$$\boldsymbol{F}^{SS} = \begin{bmatrix} 1 & \gamma & 0 \\ 0 & 1 & 0 \\ 0 & 0 & 1 \end{bmatrix} \quad \textbf{(3)} \qquad \boldsymbol{F}^{PS} = \begin{bmatrix} 1 & \gamma & 0 \\ \gamma & 1 & 0 \\ 0 & 0 & 1 \end{bmatrix} \quad \textbf{(4)}$$

Simple shear deformations are unique in their plane of deformation. The work of Holzapfel and Ogden has shown six different simple shear planes (4).
Two important quantities can be calculated from the deformation gradient tensor: The volumetric component (also known as the Jacobian) and the right-Cauchy-Green tensor. The volumetric component is then defined using standard notation,

$$J = Det(\boldsymbol{F}) \tag{5}$$

For incompressible materials $J = 1$. Furthermore, the following tensor associated with the deformation gradient,

$$\boldsymbol{C} = \boldsymbol{F}^T \boldsymbol{F} \tag{6}$$

This is the right-Cauchy-Green tensor.

It is common practice to model constitutive equations using strain energy density functions (SEDF) based on invariants of $\boldsymbol{C}$. These functions determine the energy stored in the material due to deformation. It is important for these functions to be convex in $\boldsymbol{F}$ because, therefore, they satisfy its conditions of objectivity.
The invariants used in this work are defined as follows.

$$I_1 = Tr(\boldsymbol{C}) \tag{7}$$
$$I_2 = \frac{1}{2}\left(I_1^2 - Tr(\boldsymbol{C}^2)\right) \tag{8}$$
$$I_3 = Det(\boldsymbol{C}) \tag{9}$$
$$I_4 = a^T \boldsymbol{C} a \tag{10}$$
$$I_8 = a^T \boldsymbol{C} b \tag{11}$$
$$\bar{I}_1 = J^{-2/3} I_1 \tag{12}$$
$$\bar{I}_2 = J^{-2/3} I_2 \tag{13}$$
$$\bar{I}_3 = J^{-2/3} I_3 \tag{14}$$
$$\bar{I}_4 = J^{-2/3} I_4 \tag{15}$$
$$\bar{I}_8 = J^{-2/3} I_8 \tag{16}$$

where a and b denote vectors of unit length. Therefore, these vectors present a directional dependence on the evaluation of these invariants. The invariants I_4 and I_8 are anisotropic invariants. They facilitate energy in a specific direction and the coupling between two of these directions, respectively.

2.B. Material model. The de facto constitutive law for the myocardium is the Holzapfel-Ogden model (HO-Model)(4, 10). This material model describes the hyperelastic and orthotropic behavior of the myocardium, but neglects other effects such as viscoelasticity and growth and remodeling of the tissue. This orthotropic behavior is due to the various fibers in the myocardium and their interconnection.
The SEDF of this constitutive model is defined as follows.

$$\begin{aligned}\Psi(\boldsymbol{F}) = &\frac{a}{2b}\left\{\exp\left[b\left(\bar{I}_1 - 3\right)\right] - 1\right\} \\ &+ \chi\left(\bar{I}_{4f}\right)\frac{a_f}{2b_f}\left\{\exp\left[b_f\left(\bar{I}_{4f} - 1\right)^2\right] - 1\right\} \\ &+ \chi(\bar{I}_{4s})\frac{a_s}{2b_s}\left\{\exp\left[b_s\left(\bar{I}_{4s} - 1\right)^2\right] - 1\right\} \\ &+ \frac{a_{fs}}{2b_{fs}}\left[\exp\left(b_{fs}\bar{I}_{8fs}^2\right) - 1\right] \\ &+ \frac{K}{4}\left(J^2 - 1 - 2\ln J\right)\end{aligned} \tag{17}$$

With,

$$\chi(x) = \frac{1}{1 + \exp^{-k(x-1)}} \tag{18}$$

and $k > 0$ to ensure that the function is an approximation of the Heaviside function. f and s denote the unique directions of the fiber, namely the general direction of the myofiber and the endomysial collagen. The latter is defined as the vector spanning the plane of the sheet and is perpendicular to the myofiber.
A volumetric-isochoric split of the strain energy density function is added to the original HO-model. The applied penalty function tunes the incompressibility of the material. When $K = \infty$ the material is fully incompressible. When $K = 0$ the material does not show resistance to volumetric change. Tuning of the bulk modulus is required in order to simulate (quasi-)incompressible materials because $K = \infty$ is infeasible within a computer simulation. Alternatively, lagrange multipliers can be used to independently solve for a hydrostatic pressure to enforce the incompressibility of the material. However, naive implementations can suffer from numerical convergence issues which require specialized techniques implemented in the finite

element method. One of these techniques are called hybrid elements. Such implementations were left outside of the scope of this study and thus a heuristic tuning method for the bulk modulus was adopted.

I further include an approximate Heaviside function to simulate realistic stresses due to fibrous contributions in the material. When fibers are compressed, they should not contribute to the total stress and stiffness of the material; this activation function ensures that this behavior is correctly simulated.

The SEDF tells us how much energy is stored in the material after deformation, and after taking the first and second derivative with respect to the deformation gradient, stress and stiffness measures are acquired as well. The predominant measure of stress in this work is the first Piola-Kirchoff stress (FPK or P). Contrary to other stress measures such as the second Piola-Kirchoff (SPK or S) or Cauchy (σ) stress, it possesses a simpler analytical expression. Moreover, it holds a physical interpretation by establishing a relationship between the forces acting on the deformed surface area, to the undeformed surface area. The P stress tensor can be found as follows.

$$\boldsymbol{P}(\boldsymbol{F}) = \frac{\partial \boldsymbol{\Psi}(\boldsymbol{F})}{\partial \boldsymbol{F}} \tag{19}$$

The stiffness tensor is just as easily obtained,

$$\boldsymbol{A}^{(1)}(\boldsymbol{F}) = \frac{\partial^2 \boldsymbol{\Psi}(\boldsymbol{F})}{\partial \boldsymbol{F} \partial \boldsymbol{F}} \tag{20}$$

In other texts $\boldsymbol{A}^{(1)}$ is also called the first elasticity tensor. This fourth-order tensor exhibits major, but not minor, tensor symmetries. This is indicative of duplicate entries within the tensor, which might be advantageously used to reduce computational complexity.

Although the analytical expression of the first elasticity tensor is simpler than the one obtained from S, due to the exponentials used in the HO-model, its expression still requires significant computational expense. This is due to the significant increase in the required numerical evaluations, which was facilitated by the double tensor derivative and numerous product and chain rules. In order to reduce the computational cost of working out the stiffness tensor analytically, a perturbation technique can be used to approximate the stiffness tensor (23). The approximate stiffness tensor can be found as follows.

$$\begin{aligned} A^{(1)}_{ijkl} &\approx \frac{\Delta P^{(\alpha)}_{ij}}{\Delta F^{(\alpha)}_{kl}} \approx \frac{P_{ij}\left(\mathbf{F}^{(\alpha)}_{kl}\right) - P_{ij}(\mathbf{F})}{\alpha}, \\ &\forall i,j,k,l = 1,2,3 \end{aligned} \tag{21}$$

with,

$$\mathbf{F}^{(\alpha)}_{kl} = \mathbf{F} + \Delta \mathbf{F}^{(\alpha)}_{kl} = \mathbf{F} + \alpha \overrightarrow{\mathbf{e}}_k \otimes \overrightarrow{\mathbf{e}}_l \tag{22}$$

Note that $\overrightarrow{\mathbf{e}}_k, \overrightarrow{\mathbf{e}}_l$ are unit vectors and $10^{-8} < \alpha < 10^{-6}$. In this work, the following value for α was chosen: $\alpha = 10^{-7}$.

2.C. Sample slice and fiber directions. In this work, I perform synthetic biaxial tensile tests on myocardial tissue. To this end, it is crucial to use realistic constitutive parameter values for myocardial tissue and to take into account the orientation of the sample within the ventricle to infer the direction of the fibers within the sample.

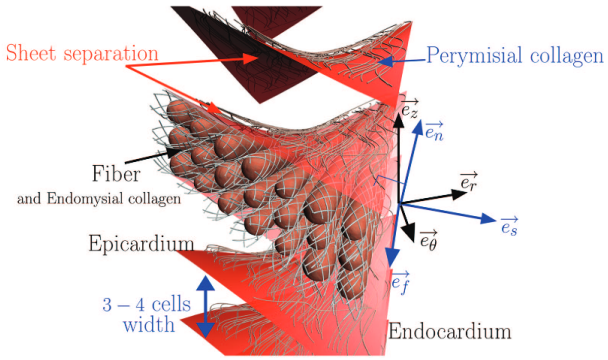

Fig. 1. This image shows the fibre angle change throughout the thickness of the ventricle. Notice that endomysial collagen envelops the fibers and interconnects them. This structure makes up a sheet. The sheet direction is subsequently found to be perpendicular to the fiber direction shown in the figure as $\overrightarrow{e_s}$ making it difficult to obtain a perfect slice. This image was obtained from (24).

During this study, the results of Rohmer et al. provide a guideline to define the sheet-like structure of the myocardium (24). In Figure 1 the mean changes in the direction of the fibers throughout the thickness of the ventricle wall and the sheet-like structure are shown. The local direction of the fiber is denoted by $\overrightarrow{e_f}$. The direction of the sheet fiber is defined to be perpendicular to the fiber direction whilst still lying within the sheet plane. It also lies approximately in the radial direction and is denoted by the vector $\overrightarrow{e_s}$. Finally, the stacking direction of the sheet is defined as $\overrightarrow{e_n}$, which is the vector normal to the sheet plane.
The orientation of these axes vary between the epicardium and endocardium, as well as in the apical and basal direction. This rotation of the fibrous sheets makes it so that the fiber distribution in each sample, as obtained similarly to the work of Sommer and Dokos (11, 12), will not be uniform. Therefore, any slice of the myocardium will have some variability in the fiber directions. However, this variability is often averaged to approximate a homogeneous material distribution within the samples.

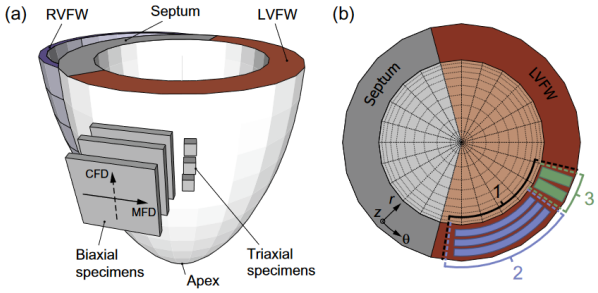

Fig. 2. (a) shows a three-dimensional image of an idealized ventricle and mechanical test samples.(b) depicts the top view of the ventricle with the current method of slicing samples for biaxial testing: (1) indicates current slices, (2) are possible for square biaxial testing and (3) is possible for the triaxial shear tests. This image was obtained from (12).

The current method of preparing myocardial tissue samples in biaxial testing setups is shown schematically in Figure 2. These samples (shown in blue) are cut from the ventricle in the circumferential direction. It is notable that the cross-fiber and mean-fiber directions are defined to lie directly in the test plane. The mean fiber direction (MFD) is defined as the general direction of the myofiber which can be equated to $\overrightarrow{e_f}$ from Figure 1. The cross-fiber direction (CFD) is defined to lie within the myocardial sheet and in the test plane which is comparable to $\overrightarrow{e_s}$, this does not correspond to the fiber orientation shown in Figure 1. According to Figure 1, the sheet direction of this commonly obtained slice should be in the radial direction.

To define the fiber direction in a simulated sample, a geometry and coordinate system must be defined. The geometry used to obtain the training data is shown in Figure 3a. It is a square sample of material with elliptical holes eclipsing in the bottom left and top right corners. These holes were added to the sample to induce heterogeneous deformation within the sample. The sides are defined to be of unit length, and both of the holes are 0.5 units long and 0.25 units wide. The x and y directions lie within the surface of the plate. In Figure 3b the side view of Figure 3a is shown. The Dirichlet boundary condition at the bottom runs across the entire surface of the sample. This ensures that the sample does not exhibit rigid body motions during the simulation. Similarly, the validation geometry is defined in Figure 4a. The side view representation is provided in Figure 4b. The validation sample has a fixed Dirichlet boundary condition applied to the bottom side, which ensures that this side will not deform in x- or y-direction during loading. The top side has a fixed displacement boundary condition applied, but also fixes its position in the x-direction to prevent the top side from contracting during deformation.

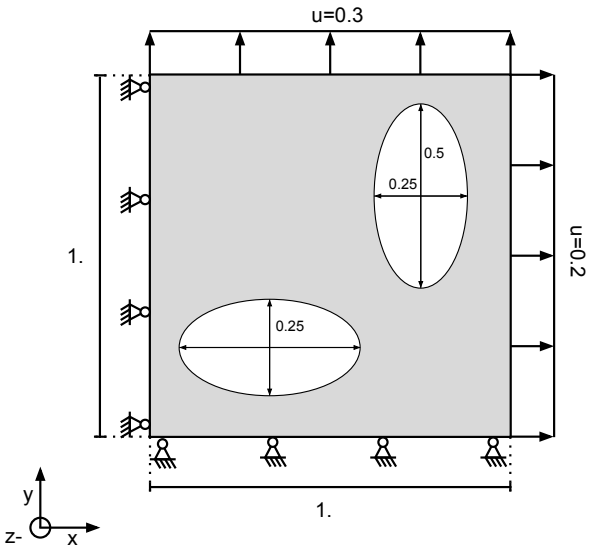

(a) The sample geometry depicted with the boundary conditions applied. Dirichlet boundary conditions are used to control the deformation of the sample. Homogeneous Dirichlet boundary conditions are found in the x- and y-directions on the bottom and left sides of the sample, respectively. On the top and right sides of the sample, fixed displacement boundary conditions are applied in y- and x-directions respectively.

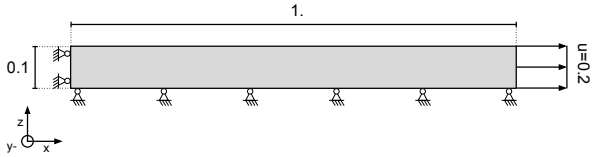

(b) The sample geometry depicted with the boundary conditions applied from a sideways perspective. The z-symmetric boundary condition on the bottom plate of the sample is clearly visible and a side view of the Dirichlet boundary conditions in x-direction provides additional perspective.

If a sample as in Figure 3a is obtained similarly to the biaxial stretch test sample in Figure 2 and using the fiber orientations defined in Figure 1, the fiber directions are defined as $f = \{0, 1, 0\}$ and $s = \{0, 0, -1\}$ in the coordinate system of the plate. These correspond to the mean-fiber direction and the sheet-fiber direction, respectively.

A problem with this type of sample is that, realistically, the fibers in the sheet direction cannot contribute to the stress or stiffness of the material under compression. Because the sample is only stretched in the x and y directions during a biaxial stretch test, the sheet fiber cannot contribute to the deformation. Therefore, attempting to retrieve information about the sheet-directional fiber will likely be intractable. Slices with such fiber orientations are called the most common slices (MCS) within the remainder of this work.

If it were possible to obtain a slice of the myocardium parallel to the sheet separations as shown in Figure 1, the fiber and endomysial collagen would lie within the test plane of the sample. In addition, the variation in the fiber orientation would be much reduced. The corresponding fiber orientations are then defined as $f = \{0, 1, 0\}$ and $s = \{1, 0, 0\}$ (or at least defined in a plane perpendicular to $\{0, 0, 1\}$) for the fiber and sheet directions, respectively. As such, it is guaranteed that biaxial stretching will pull on both fibers. However, such a slice may not be feasible to obtain because of the variation of the fibers throughout the sample and the skill required to cut parallel to these sheets. Nevertheless, displacement fields from such ideal samples might provide an upper bound of the achievable deformation modes within the sample. Slices with fiber orientations such as this are called most informative slices (MIS) in the remainder of this work.

Realistic constitutive parameter values are required to argue about the validity of this study. As such, parameter values based on experimental data were chosen. The constitutive model parameters for the HO-model used during this study were adopted from (25) and are given as $a = 0.0943$ (kPa), $b = 5.874$, $a_f = 0.311$ (kPa), $b_f = 11.271$, $a_s = 0.0431$ (kPa), $b_s = 9.772$, $a_{fs} = 0.0254$ (kPa), $b_{fs} = 2.405$. To keep the units consistent, the values in kPa are converted to Pa.

A realistic sample of the myocardium would also be nearly incompressible. Therefore, a relatively high bulk modulus value is required.

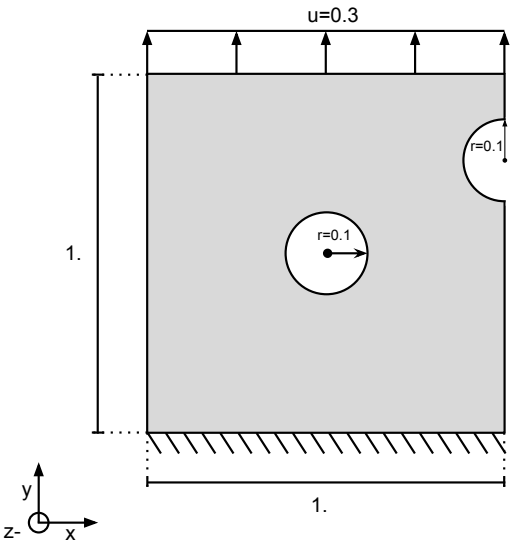

(a) The validation sample geometry depicted with the boundary conditions applied. Dirichlet boundary conditions are used to control the deformation of the sample. On the bottom side of the sample, a fixed Dirichlet boundary condition is applied. On the top side of the sample, fixed displacement boundary conditions are applied in y- and x-directions to keep the boundary from contracting in the x-axis during deformation.

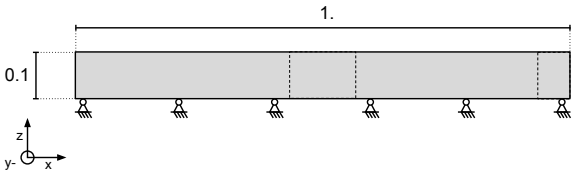

(b) The validation sample geometry depicted with the boundary conditions applied from a sideways perspective. The z-symmetric boundary condition on the bottom plate of the sample is clearly visible.

Maximum stretches at the boundary of the material must be chosen with care to stay within the physically feasible ranges of the material. I have chosen a maximum displacement in the y direction of 0.3 and the maximum displacement in the x direction of 0.2, which corresponds to those found in literature (11, 12, 14).

2.D. FEM. The finite element method (FEM) is used to simulate a material sample. In the following section, I will briefly summarize the specific formulation used in my work. In this formulation, I assume that the model will only experience Dirichlet boundary conditions, which alleviates the need for terms concerning initial stresses and external forces.
Starting with the strong form of the continuum mechanics problem,

$$DIV\{\boldsymbol{P}\} + \boldsymbol{f_0} = \boldsymbol{0} \tag{23}$$

where,

$$DIV\{\boldsymbol{P}\} = \boldsymbol{\nabla}_0 \boldsymbol{P} : \boldsymbol{I} = \frac{\partial \boldsymbol{P}}{\partial \boldsymbol{X}} : \boldsymbol{I} \tag{24}$$

with $\boldsymbol{I}$ being the second order identity tensor, $\boldsymbol{X}$ the global/undeformed spatial coordinates, and **:** being the contraction operator. Using the principle of virtual work I obtain a formulation equal to the weak form of the continuum mechanics problem,

$$\delta W = \int_V \boldsymbol{P} : \delta \dot{\boldsymbol{F}} dV + \int_V \boldsymbol{f}_0 \cdot \delta \boldsymbol{v} dV + \int_{\partial V} \boldsymbol{t}_0 \cdot \delta \boldsymbol{v} dA = 0 \tag{25}$$

where the last term corresponds to the traction forces at the boundary.
Because I will only consider a displacement-controlled tensile test, no external forces are present. To obtain a solution to this equation, I employ an iterative Newton-Rhapson solver. To this end, a linearized version of the aforementioned equation needs to be found. Using the directional derivative the following step can be taken,

$$\begin{aligned} D\delta W[u] &= \int_V D\boldsymbol{F}[u] : \boldsymbol{A}^{(1)} : \nabla_0 \boldsymbol{u} dV + \int_V \boldsymbol{P} : \nabla_0 \delta \boldsymbol{v} dV \\ &= \int_V \nabla_0 \delta \boldsymbol{v} : \boldsymbol{A}^{(1)} : \nabla_0 \boldsymbol{u} dV + \int_V \boldsymbol{P} : \nabla_0 \delta \boldsymbol{v} dV = 0 \end{aligned} \tag{26}$$

where $D \cdot [u]$ denotes the directional derivative in direction u and ∇_0 denotes the partial derivative w.r.t. the initial configuration. Since the second term in the linearized equation defines the initial stresses in the configuration, which were considered not to be present, this term is neglected.
Finally, the problem can be discretized using $\boldsymbol{u} = \sum_{a=1}^{n} N_a \boldsymbol{u}_a$ and the result is stated as

$$
\begin{aligned}
D\delta W^e[u] &\approx \int_{V_e} \nabla_0 \sum_{a=1}^{n} N_a \delta \boldsymbol{v}_a : \boldsymbol{A}^{(1)} : \nabla_0 \sum_{b=1}^{n} N_b \delta \boldsymbol{u}_b dV \\
&= \delta \boldsymbol{v}_a \cdot \boldsymbol{K}_{ab}^{(e)} \boldsymbol{u}_b
\end{aligned} \tag{27}
$$

where n is the number of nodes per element and e denotes the specific element used. Integrating over the volume using Gauss quadratures, the global tangent matrix can be assembled, and the standard formulation for a Newton-Rhapson problem emerges,

$$
\boldsymbol{K}(\boldsymbol{X}; \boldsymbol{u}_{k-1}) \boldsymbol{u}_k = -\boldsymbol{R}(\boldsymbol{X}; \boldsymbol{u}_{k-1}) \tag{28}
$$

where we see that the tangent stiffness matrix and the residual R are both dependent on the initial configuration as a constant parameter and the displacement vector $\boldsymbol{u}_{k-1}$ which is initialized at zero barring the nodes undergoing Dirichlet boundary conditions. The residual is found by discretizing equation 25 in a manner similar to that for the tangent stiffness matrix.

Using the discrete equations defined above, the geometry of the sample, and the accompanying boundary conditions, a solution to the finite element problem can be obtained using an adequate mesh of the geometry. The meshed geometry contained 11895 elements and 15228 nodes. The elements chosen for the purpose of this study were linear brick elements (C3D8). These elements satisfy the Kronecker-δ property and thus physically represent the displacement field. This mesh was chosen based on the results of a mesh convergence study (see Appendix A). During this process, the bulk modulus was gradually increased until the simulation failed to converge. The value was then reduced to the last feasible one. In so doing, I settled on a bulk modulus value of 1500. The material was stretched in x- and y-directions through nonhomogeneous Dirichlet boundary conditions, recreating the biaxial tensile test. The boundary conditions were increased linearly to aid in the convergence of the method. Step sizes for this increase were set at fixed intervals, allowing for the recording of snapshots over time of the converged solution.

2.E. Full field approximation. In an ideal setting, the whole force and deformation field would be known to the user (the full field or FF setting). However, in practice, this is not the case. Forces can only be measured at the boundary and only in rough patches. It is assumed that only the sum of the forces on each side of the sample can be measured. The finite element method provides solutions for the displacement at each node in the mesh. As a result, the entire displacement field is known. Using the solution directly will be referred to as using the full-field measurements for the deformation.

The deformation field can also be obtained by means of Digital Image Correlation (DIC). This approach results in a deformation field with relatively high precision of the top surface of the sample. When considering thin samples, these top-surface measurements are assumed to be characteristic of the whole material.

A classical DIC setup can only provide planar deformation measurements, and information about a change in thickness of the sample is not measured. Stereo DIC (SDIC) approaches attempt to remedy this by using two different viewing angles and comparing the images to infer depth. Again, these measurements pertain only to the top surface of the material.

In this work, a fictitious method is proposed that approximates the full mesh and the corresponding deformation field from SDIC measurements alone. The thickness of the sample is assumed to be measured beforehand, and the method linearly interpolates the deformations of the top surface to the bottom surface lying in the $z = 0$ plane. All deformations in the x and y axes are imposed on the underlying nodes.

A function interpolating the deformation throughout the mesh is given in equation 29,

$$
\boldsymbol{\phi}_a^i = \begin{bmatrix} 1 & 0 & 0 \\ 0 & 1 & 0 \\ 0 & 0 & 1 - \frac{N_L - a - 1}{N_L - 1} \end{bmatrix} \boldsymbol{\phi}_{top}^i, \quad \forall a \in \{1, 2, \cdots, N_L - 1\} \tag{29}
$$

Where N_L denotes the number of required layers in the mesh and a the index of the nodes directly below the mesh of the top-surface. ϕ denotes the field variable and can be the original coordinates in $\boldsymbol{X}$ or the deformation field $\boldsymbol{u}$. A schematic overview of the aforementioned approach can be seen in Figure 5.

Using both full displacement field measurements and the aforementioned SDIC approach along with the two considered slicing directions, four resulting data-sets are obtained. For the remainder of this work, the following abbreviations will be used: FF-MIS, SDIC-MIS, FF-MCS, and SDIC-MCS. FF-MIS stands for the use of the full displacement field measurements of a deformed sample cut in the most informative slicing direction. SDIC-MIS uses the same slicing direction but uses the SDIC measurement technique. FF-MCS stands for the use of full displacement field measurements of a sample cut in the most common slicing direction. SDIC-MCS uses the same slicing direction as FF-MCS, but uses the SDIC measurement technique.

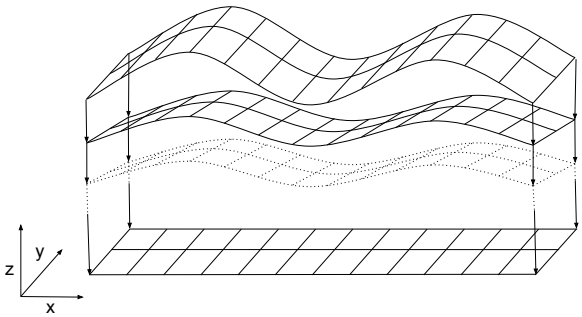

Fig. 5. A graphic showing how the top surface is copied n times until it hits the bottom plate where $z = 0$. The deformations at the top surface are propagated through the mesh by assuming that the x- y- displacements are the same throughout the thickness of the mesh. The deformation in the z-direction is assumed to converge to zero at the bottom plate of the mesh.

2.F. Bayesian-EUCLID. Bayesian-EUCLID is an unsupervised machine learning algorithm used to identify constitutive material laws based on displacement and force data. This type of data is readily available from standard tensile testing setups and therefore makes the method directly applicable to this study.

The objective of the algorithm is to find a strain energy density function that maintains the linear momentum balance. The exact material model is unknown to the algorithm, but is provided with a material-model/feature library. These features are commonly found in constitutive equations and inherently satisfy polyconvexity constraints that are necessary for material objectivity and stability. Such features are derived from the aforementioned strain invariants while ensuring that the feature contributes no energy while in the reference configuration.

The following feature library is used in this work,

$$\begin{aligned}
&\boldsymbol{Q}\left(I_1, I_2, I_3, I_4, I_8\right) = \\
&\underbrace{\left[\left(\bar{I}_1 - 3\right)^i \left(\bar{I}_2 - 3\right)^{j-i} : i \in \{0, \ldots, j\} \text{ and } j \in \{1, \ldots, N_{\mathrm{MR}}\}\right]^T}_{\text{Generalized Mooney-Rivlin features}} \\
&\oplus \underbrace{\left[\left(J^2 - 1 - 2ln(J)\right)\right]}_{\text{Volumetric energy feature}} \oplus \left[\left(\bar{I}_{4f} - 1\right)^i : i \in \{2, \ldots, N_{\text{aniso}}\}\right] \\
&\oplus \left[\left(\bar{I}_{4s} - 1\right)^i : i \in \{2, \ldots, N_{\text{aniso}}\}\right] \\
&\oplus \left[\left(\bar{I}_{8fs}\right)^i : i \in \{2, \ldots, N_{\text{aniso}}\}\right]
\end{aligned} \tag{30}$$

Where $\oplus$ denotes the concatenation of the features. It is noteworthy that the set does not contain the exponential invariants of I_1, I_{4f}, I_{4s}, or I_{8fs} found in the ground truth material model in equation 17. Instead, polynomials of these features are provided. Therefore, this feature set can only approximate the ground truth material model. The strain energy density is subsequently determined through

$$W(I_1, I_2, I_3, I_4, I_8) = \boldsymbol{Q}(I_1, I_2, I_3, I_4, I_8) \cdot \boldsymbol{\theta} \tag{31}$$

EUCLID enforces physically meaningful results by inherently satisfying the equilibrium constraints of the material. It does so by finding parameter values for the weak form of the linear momentum balance,

$$\int_\Omega \boldsymbol{P} : \nabla \boldsymbol{v} \mathrm{d}V + \int_{\partial\Omega_t} \boldsymbol{t} \cdot \boldsymbol{v} \mathrm{d}S = 0, \quad \forall \quad \text{admissible } \boldsymbol{v} \tag{32}$$

Notice the similarity with equation 25. There is an equivalence between the two if the following is considered: $\dot{\boldsymbol{F}} = \nabla_0 \delta v$. Now using the following discretization for the test function $\boldsymbol{v}$,

$$\boldsymbol{v} = \sum_{a=1}^{n} N_a \boldsymbol{v}_a \tag{33}$$

Then the linear momentum balance reduces to

$$\sum_{a=1}^{n} \boldsymbol{v}_a \left[\int_\Omega \boldsymbol{P} \nabla N_a \mathrm{d}V + \int_{\partial\Omega_t} \boldsymbol{t} N_a \mathrm{d}S\right] = 0 \tag{34}$$

Now apply equation 19 to equation 31 and substitute the result into equation 34,

$$\sum_{a=1}^{n} \boldsymbol{v}_a \left[\int_{\Omega} \left(\frac{\partial Q}{\partial F_{ij}} \boldsymbol{\theta} \right) \nabla_j N_a \mathrm{d}V + \int_{\partial \Omega_t} \boldsymbol{t}_i N_a \mathrm{d}S \right] = 0 \tag{35}$$

Because $\boldsymbol{\theta}$ does not depend on the spatial coordinates, it is taken outside of the integral. After applying numerical integration through Gaussian quadrature, the resulting set of linear equations can be written as

$$\boldsymbol{A}^{free} \boldsymbol{\theta} = \boldsymbol{b}^{free} \tag{36}$$

The balance must also be maintained at the boundary. To this end, the aggregated internal forces must match the external force,

$$\begin{aligned} &\sum_{(a,i) \in \mathcal{D}^{\mathrm{fix},\beta}} F_i^{\mathrm{int},a}(\boldsymbol{\theta}) = \\ &\sum_{(a,i) \in \mathcal{D}^{\mathrm{fix},\beta}} \int_{\Omega} \left(\frac{\partial Q}{\partial F_{ij}} \boldsymbol{\theta} \right) \nabla_j N_a \mathrm{d}V = \\ &\sum_{(a,i) \in \mathcal{D}^{\mathrm{fix},\beta}} F_i^{\mathrm{ext},a} = R^{\beta}, \quad \forall \quad \beta = 1, \ldots, n_{\beta}, \end{aligned} \tag{37}$$

Which can be assembled in the same way as in the finite element method. After concatenating the results, the following relationship emerges.

$$\boldsymbol{A} \boldsymbol{\theta} = \boldsymbol{b} \tag{38}$$

with,

$$\boldsymbol{A} = \begin{bmatrix} A^{\mathrm{free},1} \\ \vdots \\ A^{\mathrm{free},n_t} \\ \lambda_r A^{\mathrm{fix},1} \\ \vdots \\ \lambda_r A^{\mathrm{fix},n_t} \end{bmatrix}, \boldsymbol{b} = \begin{bmatrix} b^{\mathrm{free},1} \\ \vdots \\ b^{\mathrm{free},n_t} \\ \lambda_r b^{\mathrm{fix},1} \\ \vdots \\ \lambda_r b^{\mathrm{fix},n_t} \end{bmatrix}, \tag{39}$$

Where $\lambda_r > 0$ is the hyperparameter controlling the relative importance of the force balance between the fixed and free degrees of freedom. The number of degrees of freedom is usually equal to the amount available in the simulation, but in Bayesian-EUCLID this value can be tuned. This allows the method to work with fewer datapoints, which improves the computational efficiency.
Due to uncertainties in the displacements, uncertainties also exist in $\boldsymbol{A}$. Therefore, a better description is

$$\boldsymbol{A} \boldsymbol{\theta} = \boldsymbol{b} + \boldsymbol{\epsilon} \tag{40}$$

Where $\boldsymbol{\epsilon}$ denotes the residual of the momentum balance and is indicative of the uncertainty in both the measurements and the model. It is assumed that the residual can be sampled i.i.d. from a normal distribution as

$$\boldsymbol{b} \mid \boldsymbol{\theta}, \sigma^2, \boldsymbol{A} \sim \mathcal{N}\left(\boldsymbol{A}\boldsymbol{\theta}, \sigma^2 \boldsymbol{I}_N \right) \tag{41}$$

Finally, the stochastic model formulation used in Bayesian-EUCLID is found. The model can now be solved for $\boldsymbol{\theta}$ by calculating the posterior distribution of $\boldsymbol{\theta}$ given prior information on $\boldsymbol{\theta}$, $\boldsymbol{A}$, as well as the likelihood of $\boldsymbol{b}$.
The method enforces sparse results through spike-slab priors. This type of prior has a high probability that the value of $\boldsymbol{\theta}$ is (near) zero and a small probability that it lives in $\mathbb{R}^+$. By selecting just a few active features during each sampling iteration of the algorithm using a probability distribution, a distinction can be made between the features. This distinction concerns the contribution to maintaining the linear momentum balance. If the feature does not contribute (much), it will be selected fewer times in subsequent iterations.

$$\begin{aligned} z_i \mid p_0 &\sim Bern(p_0) && \text{(i.i.d. Bernoulli trial)} \\ \nu_s &\sim \mathcal{IG}(a_\nu, b_\nu) && \text{(Inverse Gamma distribution)} \\ \sigma^2 &\sim \mathcal{IG}(a_\sigma, b_\sigma) && \text{(Inverse Gamma distribution)} \\ p_0 &\sim Beta(a_p, b_p) && \text{(Beta distribution)} \end{aligned} \tag{42}$$

The types of distribution used to define the spike-slab priors are given in Equation 42. The relationship between these distributions and the a priori information is schematically shown in Figure 6, which has been adopted from the Bayesian-EUCLID paper (22). Using these distributions, the definition of the posterior distribution is found as follows.

$$p\left(\boldsymbol{\theta}, z, p_0, v_s, \sigma^2 \mid \boldsymbol{A}, \boldsymbol{b}\right) \propto \underbrace{p\left(\boldsymbol{b} \mid \boldsymbol{\theta}, \boldsymbol{z}, p_0, v_s, \sigma^2, \boldsymbol{A}\right)}_{\text{physics-constrained likelihood}} \underbrace{p\left(\boldsymbol{\theta}, \boldsymbol{z}, p_0, v_s, \sigma^2\right)}_{\text{spike-slab model prior}} \tag{43}$$

Because it is infeasible to sample from an analytical solution to this problem, a Markov chain Monte Carlo (MCMC) method is required. The posterior distribution of the model is estimated using a Gibbs sampler.

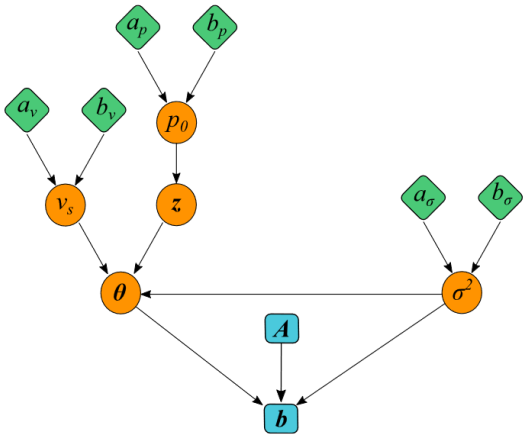

Fig. 6. This figure shows the relationship between the prior distributions and the a priori information $\boldsymbol{A}$ and $\boldsymbol{b}$. This matrix $\boldsymbol{A}$ and vector $\boldsymbol{b}$ maintain the linear momentum balance and are directly derived from the feature-set and the deformation field. This image has been adopted from (22).

Using the average value of $Z_{activity}$, a preferred set of features can be found by comparing the average value against a cutoff value.

$$Z_{avg} = \frac{1}{N_G} \sum_{i=1}^{N_G} z_i \tag{44}$$

where $N_G = N_{links} - N_{burn}$,

After selecting the preferred features and discarding the previous results, the algorithm can be run again to obtain more accurate and sparse results. This is a recursive process and is limited by the stringency of the cutoff value, the desired sparsity of the model, and the importance of the force balance through λ_r. This process was inspired by (26), who used a similar approach to determine a posterior inclusion probability for each feature in the set.

A set of hyperparameter values was heuristically fitted using the results of the experiment which included the full deformation field and the most informative slice (FF-MIS). The main consideration of this fitting procedure was the ability to obtain a sparse model which (if possible) included all desired features ($(I_1 - 3)$, $(I_{4f} - 1)$, $(I_{4s} - 1)$, (I_{8fs}), and the volumetric feature). Further considerations included the ability of the algorithm to construct nonsingular matrix $\boldsymbol{A}$ (equation 39) as the presence of singular matrices would terminate the algorithm. To achieve this, the value of λ_r was increased until singular matrices were constructed. Subsequently, the value was reduced by a factor of 10, which generally performed well. The number of included degrees of freedom in the algorithm was qualitatively determined by the variance of the obtained parameter value. Increasing this value produced results with lower variance but also with a considerable increase in computational complexity.
The summary of all the parameters used in the FEM data generation and the model discovery through Bayesian-EUCLID can be found in table 1 in Appendix B.
In order to better argue about the differences in the obtained models, the hyperparameters heuristically fitted onto the FF-MIS forward simulation results were also used on the remaining three results: SDIC-MIS, FF-MCS, and SDIC-MCS.

3. Results

3.A. Forward Simulations. Seven forward simulations are performed during this work, two of which are simulations of the HO-model with different fiber orientations for the training data. The remaining simulations are related to the validation

specimen. The first of these five simulations serves as a ground-truth for the validation specimen, and it is therefore simulated using the HO-model. To ensure that both fibers are stretched in this uniaxial stretch test, the MIS fiber orientation is rotated another 30 degrees around the z-axis. The remaining four simulations use the approximated models. In order to compare against the ground truth of the validation sample, all of these material models make use of the same fiber orientation as the ground-truth model.

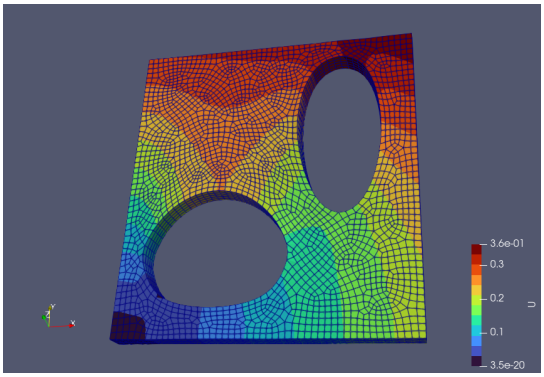

Fig. 7. Mesh of the training sample undergoing biaxial stretch testing. This sample is obtained through simulating the ground truth HO-model in the MIS direction. Thus, the main fiber direction lies directly in the y-axis and the sheet fiber direction in the x-axis.

In Figure 7 we can observe the heterogeneous deformation field in the material due to the biaxial tensile test. The sample was stretched in the y direction for 30% of its initial length, and for 20% of its initial length in the x direction. The top, bottom, left, and right sides of the sample were subjected to simple Dirichlet boundary conditions. A final Dirichlet boundary condition was enforced in the z direction for the entire bottom plate of the sample to keep the sample from exhibiting rigid body motions.

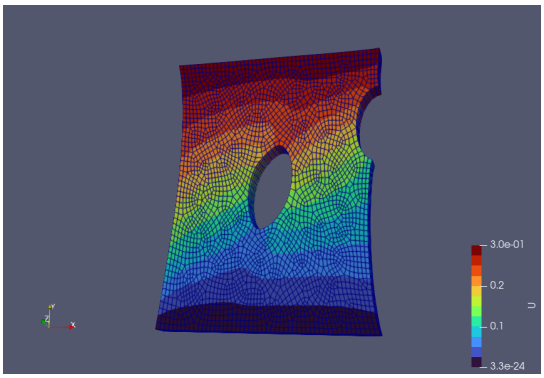

Fig. 8. The deformed validation sample. This asymmetrical geometry provides heterogeneous deformations which facilitates the validation of the approximated model to generalize to unseen data. This deformed version of the validation sample was obtained through a finite element analysis using the ground truth HO-model where both fibers lie in the plane, but instead of pointing directly in the x and y axis, they are rotated around the z-axis with 30 degrees. This ensures that both fibers are stretched in the uniaxial test.

In Figure 8 we can observe the heterogeneous deformation field in the material due to the uniaxial tensile testing. The sample was stretched in the y direction for 30% of its initial length. The top and bottom of the sample underwent z-asymmetric Dirichlet boundary conditions. These boundary conditions fix the displacement on all axes but on the z-axis. The left and right sides of the sample were free of boundary conditions. A final Dirichlet boundary condition was enforced in the z direction for the entire bottom plate of the sample to keep the sample from exhibiting rigid body motion.

3.B. Bayesian-EUCLID models. Three graphs are considered in this section: Violin plots, deformation path energies, and activity plots. The violin plots represent the normalized probability density around the mean parameter values. On the bottom x-axis, the retrieved features are listed. The upper x-axis shows the corresponding mean parameter value of the feature. The colored areas show the probability density of the parameter values. Therefore, violins with a large area show greater uncertainty around the parameter value obtained.

In order to add an estimate of the predictive capabilities of the approach, I determined the energies along specific and homogeneous deformation paths of the ground-truth material model and the approximated models. These deformation paths consist of Uniaxial Tension (UT), Biaxial Tension (BT), and six different simple shear modes (FS, SF, FN, NF, NS, SN). The names of these shear modes refer to the plane in which the deformation takes place. In this case, F stands for the mean direction of the fiber, or y in the coordinate system used in Figure 3a. S represents the direction of the sheet fiber, or x in the coordinate system, and N represents the direction of the cross fiber, which is the same as the z direction in the coordinate system. This is

analogous to the notation used in (4). The strain energy density function is then evaluated for each model along the deformation path. Examples of such paths are shown in equations 1, 2, 3, and 4 where the path is evaluated along the variable γ. The red lines in the graph indicate the energies obtained from the ground-truth HO-model, and the black lines show the mean of the approximated model. The gray area around these black lines shows the 95 percentile values. Therefore, the spread of this area represents the uncertainty in the prediction of the energy density. To quantify the prediction accuracy, the coefficient of determination (R^2) between the black and red lines is calculated and presented in each of these graphs. The definition of this value is given below.

$$R^2 = 1 - \frac{\sum_i \left(y_{\text{true, i}} - y_{\text{pred, i}}\right)^2}{\sum_i \left(y_{\text{true, i}} - \overline{\boldsymbol{y}_{\text{true}}}\right)^2} \tag{45}$$

Where $y_{\text{true, i}}$ denotes the true value and $y_{\text{pred, i}}$ denotes the predicted value.

Lastly, the activity plots show the progression of feature selection over the iterations of the Bayesian-EUCLID approach. Because the value of z is 1 or 0, the value on the bar graph shows the percentage of models in which the corresponding feature was used. The blue bars show the average activity of the features in the first iteration of this approach. The orange bars show this average activity for the second iteration. The red horizontal line shows the cutoff value used to reduce the posterior feature set before it is used in the second iteration.

B.1. FF-MIS results. First, the full deformation field is considered. In this scenario, no approximation methods are employed for the deformation field. In other words, the results from the finite element analysis are directly presented to the Bayesian-EUCLID method.

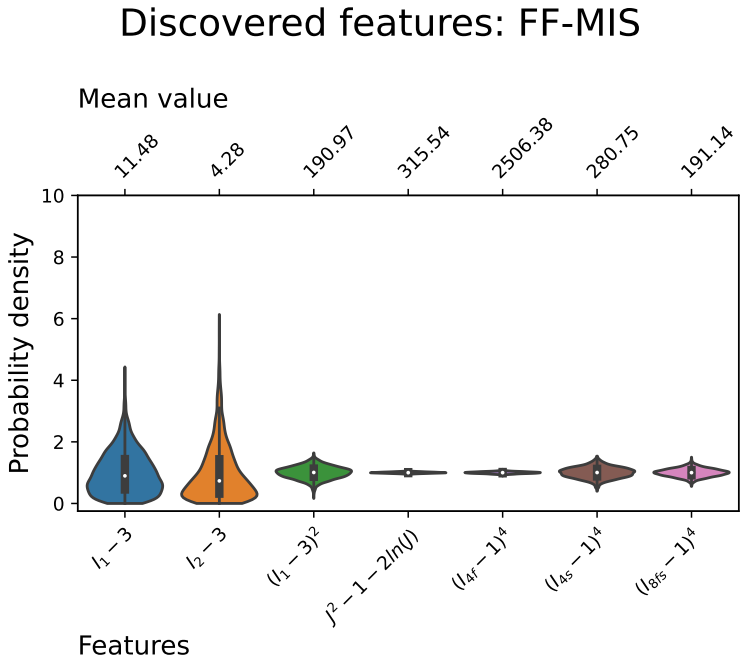

Fig. 9. Results from the Bayesian-EUCLID algorithm when using the most informative slice and a full deformation field. The y axis shows the normalized probability density of the distribution. Large deviation from 1 therefore means a high standard deviation. The bottom x axis shows the constitutive model feature discovered by the algorithm from its initial feature set. The top x axis shows the mean parameter value corresponding to the discovered feature.

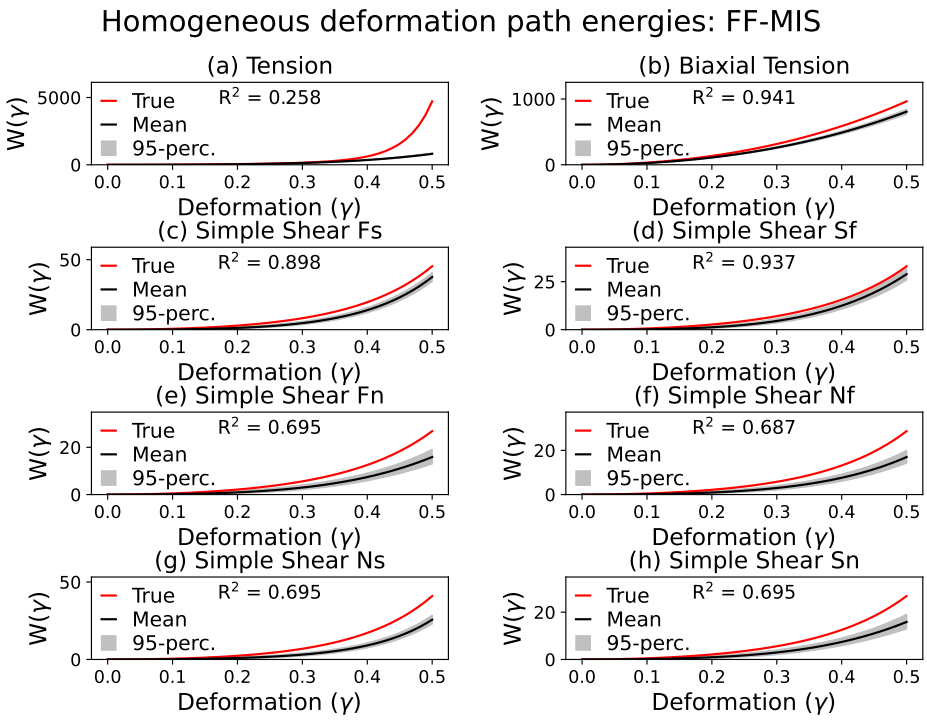

Fig. 10. The ground truth energies compared to the predicted model energies due to imposed deformation gradients. These results were obtained using the full deformation field and the most informative slice of the myocardium.

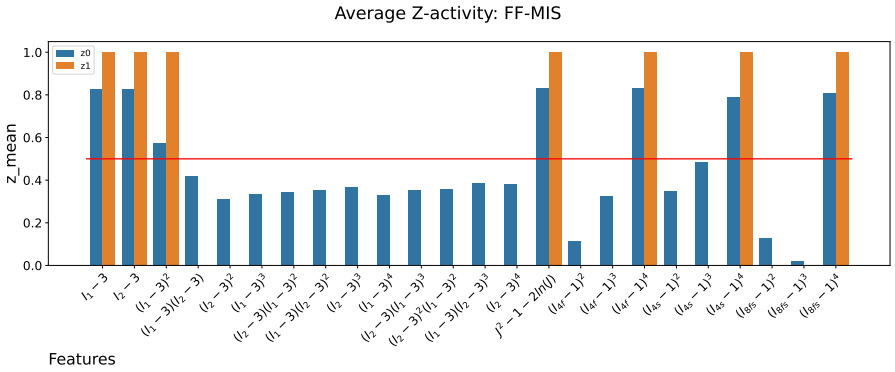

Fig. 11. The mean values of the z activity for both iterations when considering the full field information case using the most informative slice.

In Figure 9, a violin plot shows the retrieved features for the approximated model of the FF-MIS data set. From the bottom x-axis it can be seen that the method was capable of retrieving the following features: I_1-3, I_2-3, $(I_1-3)^2$, $J^2-1-2ln(J)$, $(I_{4f}-1)^4$, $(I_{4s}-1)^4$, and $(I_{8fs})^4$. The first two show larger uncertainties around their parameter values. It is noteworthy that all other features, especially the volumetric and $(I_{4f}-1)^4$, show a relatively low uncertainty.

An estimate of the predictive capabilities of the approximated model is presented in Figure 10. In this figure, the $\boldsymbol{R}^2$ values for graphs (b), (c), and (d) are above 0.89. Such values, which are close to 1, show a good correspondence with the true value. From a qualitative standpoint, it can be seen that the black lines follow the ground truth (in red). The graphs (a), (e), (f), (g), and (h) show that the mean predicted value deviates substantially from the ground truth. The corresponding $\boldsymbol{R}^2$ values are also considerably lower and are around 0.69. Nevertheless, the 95 percentile areas are qualitatively small and therefore agree well with the variance seen in the violin plots.

In Figure 11 the progression of the feature selection is shown. This figure shows that a large number of features are removed after the first iteration. The remaining feature activities stabilize during the second iteration, since their average value is equal to 1.

B.2. SDIC-MIS results. The second data set contains the SDIC measurements of the FEM results using the most informative slicing direction. This approximation of the deformation field is fed into the Bayesian-EUCLID method and produced the following results:

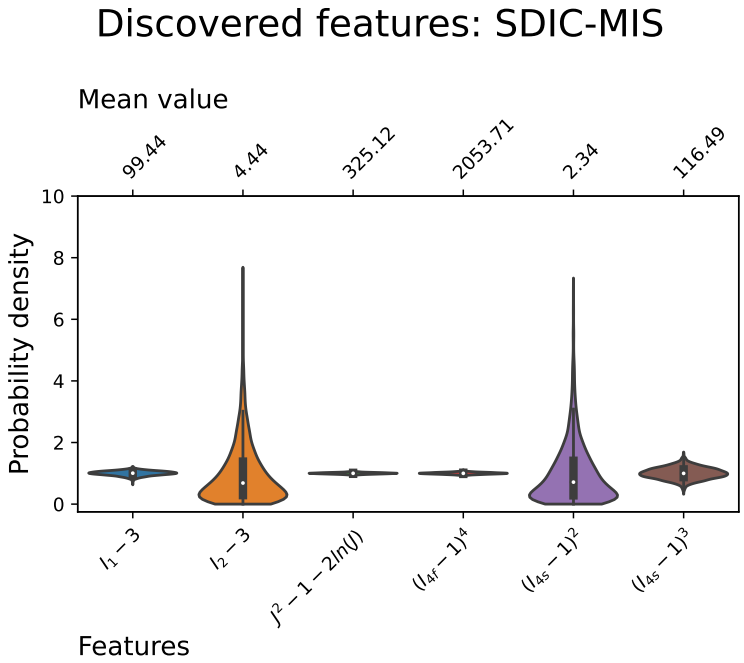

Fig. 12. Violin plot of the most informative slice and its discovered features while using the 2.5D approximation.

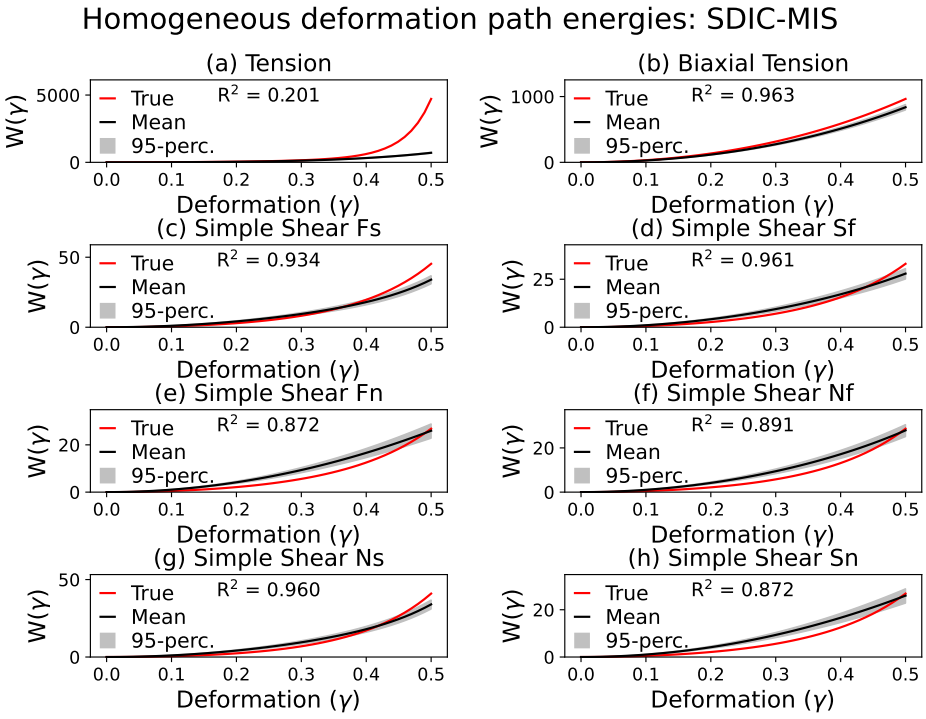

Fig. 13. The ground truth energies compared to the predicted model energies due to imposed deformation gradients while using the 2.5D approximation of the most informative slice.

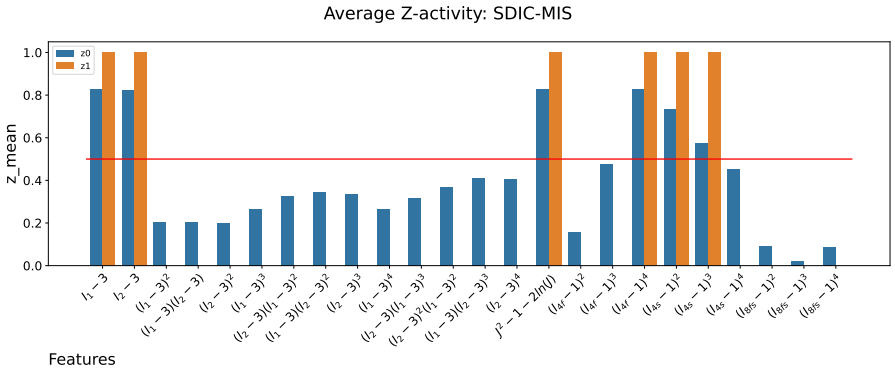

Fig. 14. The mean values of the z activity for both iterations considering the 2.5D approximation of the deformation field of the most informative slice.

The violin plot in Figure 12 shows a sparse approximate model. On the bottom x-axis, the following features are available: $I_1 - 3$, $I_2 - 3$, $J^2 - 1 - 2ln(J)$, $(I_{4f} - 1)^4$, $(I_{4s} - 1)^2$, and $(I_{4s} - 1)^3$. Compared to the results in Figure 9, no fiber-coupling terms containing I_{8fs} are found. Furthermore, the polynomial order in $(I_{4s} - 1)$ has been reduced from 4 to 3 and the polynomial order in $I_1 - 3$ is reduced from 2 to 1. It is also noteworthy that the parameter values of the highest polynomial order of each feature have a similar order of magnitude.

The energy plots in Figure 14 show a relatively high value for R^2 that ranges from 0.872 to 0.977. Compared to the R^2 values presented in Figure 10, these are higher. The 95 percentile areas (colored gray) presented in this graph are small. This shows that the model is relatively certain about its prediction.

The progression of the feature selection presented in Figure 14, clearly shows that even in the first iteration of the algorithm, the sheet coupling features have a low average activity value. The features $(I_{4f} - 1)^3$ and $(I_{4s} - 1)^4$ have an average activity value just below the cutoff value. The other average activity values are substantially below the cutoff value and are also rejected after the first iteration. This greatly reduced set of features converges in feature activity since all features have an average activity of 1.

B.3. FF-MCS results. Now the most common slicing direction is considered. Using the full deformation field, the following results are obtained.

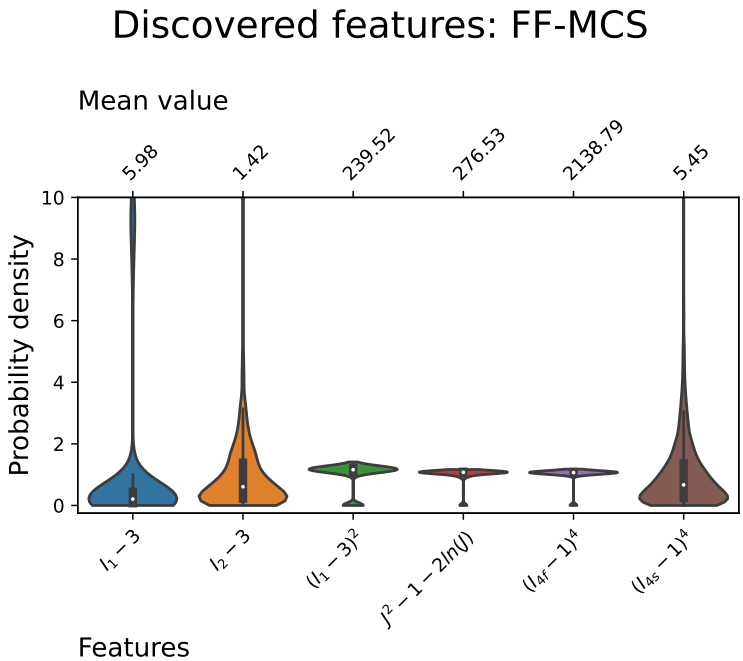

Fig. 15. Results from the Bayesian-EUCLID algorithm when using the common slice and a full deformation field. The y axis shows the normalized probability density of the distribution. Large deviation from 1 therefore means a high standard deviation. The bottom x axis shows the constitutive model feature discovered by the algorithm from its initial feature set. The top x axis shows the mean parameter value corresponding to the discovered feature.

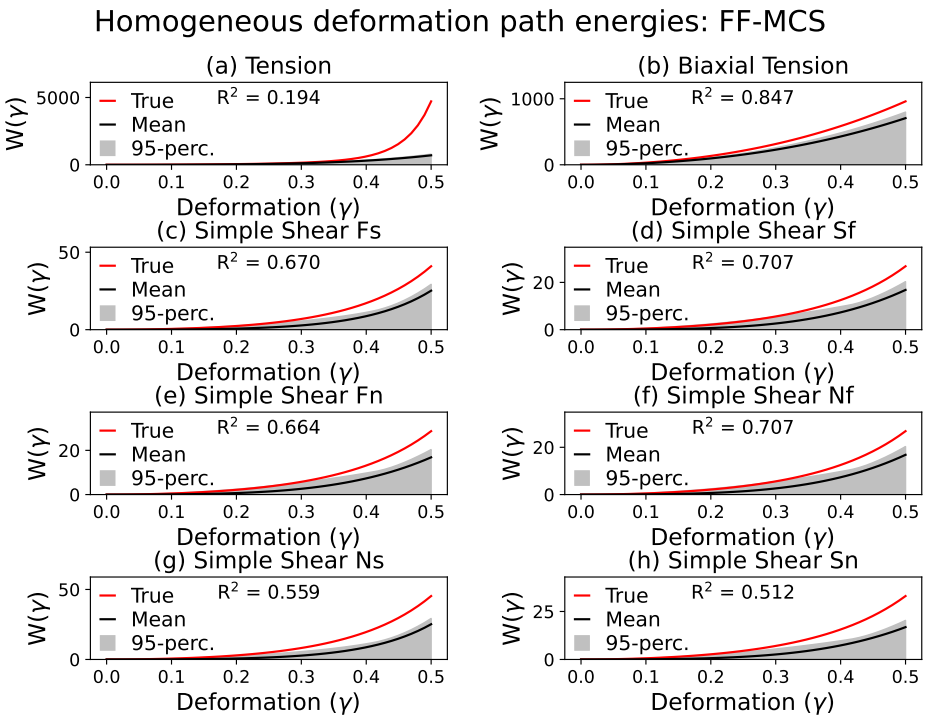

Fig. 16. The ground truth energies compared to the predicted model energies due to imposed deformation gradients of the most common slice with its full deformation field being used in the Bayesian-EUCLID algorithm.

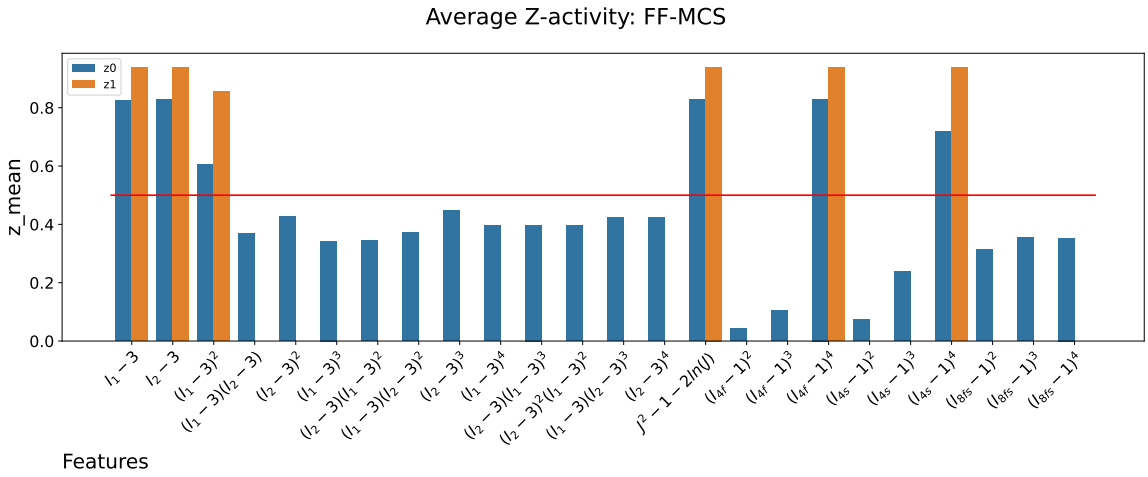

Fig. 17. The average z activity of the Markov chain when considering the most common slice and using the full deformation field.

The violin plot in Figure 15 shows another sparse material model. The following features are present in the model: I_1-3, I_2-3, $(I_1-3)^2$, $J^2-1-2ln(J)$, $(I_{4f}-1)^4$, and $(I_{4s}-1)^4$. The features I_1-3, I_2-3, and $(I_{4s}-1)^4$ show large areas and therefore denote a relatively large uncertainty about their parameter value. Their areas are also truncated at zero, indicating that the probability that this parameter value equals zero is high in this obtained model. When the violins of the features $(I_1-3)^2$, $J^2-1-2ln(J)$, and $(I_{4f}-1)^4$ are compared to those from Figure 9, small stems and protrusions at 0 are notable. The probability density distribution of these features is multimodal, because even though the bulk of the area of these violins is centered around their mean, a small portion is still visible at zero.

The effects of this multimodality are noticed in Figure 16. Large 95 percentile areas are visible which range from 0 to just above the mean. The R^2 values range from 0.512 to 0.707 for the shear modes and from 0.812 to 0.847 for the tension modes. Compared to those of the previous graphs, which ranged from 0.872 to 0.977 in the approximate case and from 0.69 to 0.941 in the full-field case, they are considerably lower.

The progression of the feature selection method in Figure 17 shows that the set of features is drastically reduced after the first iteration. The average activity of the remaining features stabilizes for all but the $(I_1-3)^2$ feature, which has a value between 0.8 and 1.

B.4. SDIC-MCS results. The last approximate model made use of the SDIC measurements of the MCS FEM results.

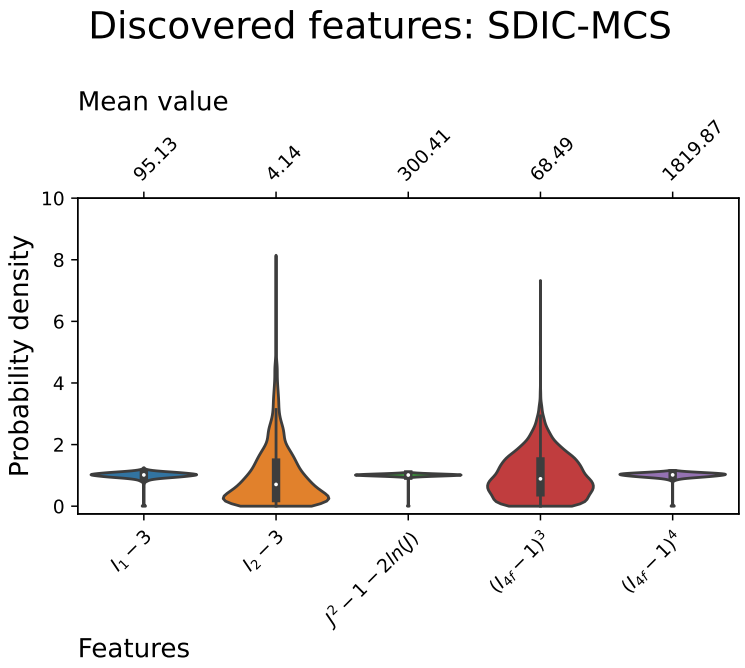

Fig. 18. Violin plot of the most common slice and its discovered features when using the 2.5D approximation of the deformation field.

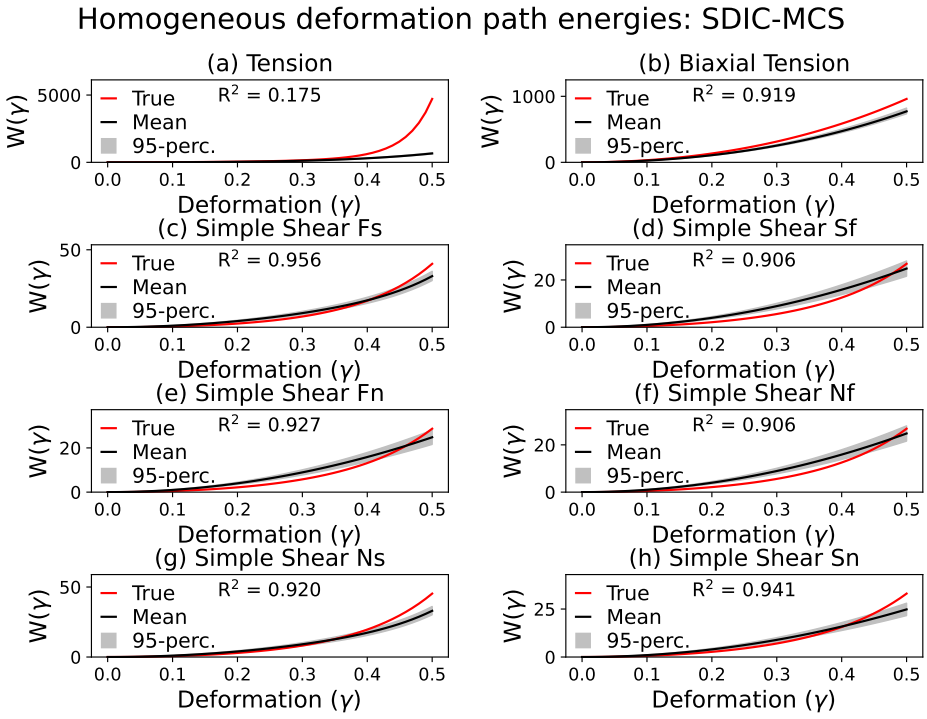

Fig. 19. The ground truth energies compared to the predicted model energies due to imposed deformation gradients when considering the most common slice and the 2.5D approximation of the deformation field.

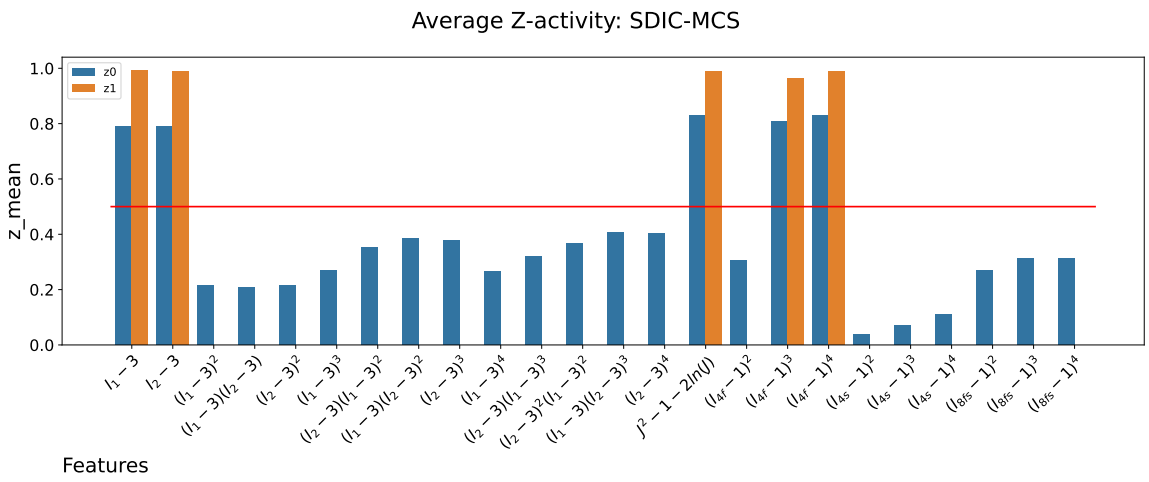

Fig. 20. The ground truth energies compared to the predicted model energies due to imposed deformation gradients when considering the most common slice and the 2.5D approximation of the deformation field.

The violin plot in Figure 18 shows another parsimonious material model. It contains the following five features: $I_1 - 3$, $I_2 - 3$, $J^2 - 1 - 2ln(J)$, $(I_{4f} - 1)^3$, and $(I_{4f} - 1)^4$. Relatively large variance is observed only in the features $I_2 - 3$ and $(I_{4f} - 1)^3$.

The energy path predictions in Figure 19 qualitatively show that they can follow the ground truth. The accompanied R^2 values also show relatively high values. These range from 0.906 to 0.956.

The progression of the feature selection procedure shown in Figure 20 indicates that the method was already quite certain of the features to be included in the approximate model. The features not included in the second iteration have considerably lower average activity values than the cut-off value. All features included in the final model, except for the $(I_{4f} - 1)^3$ feature, stabilize as they have an average activity of 1. The $(I_{4f} - 1)^3$ feature has a slightly lower value.

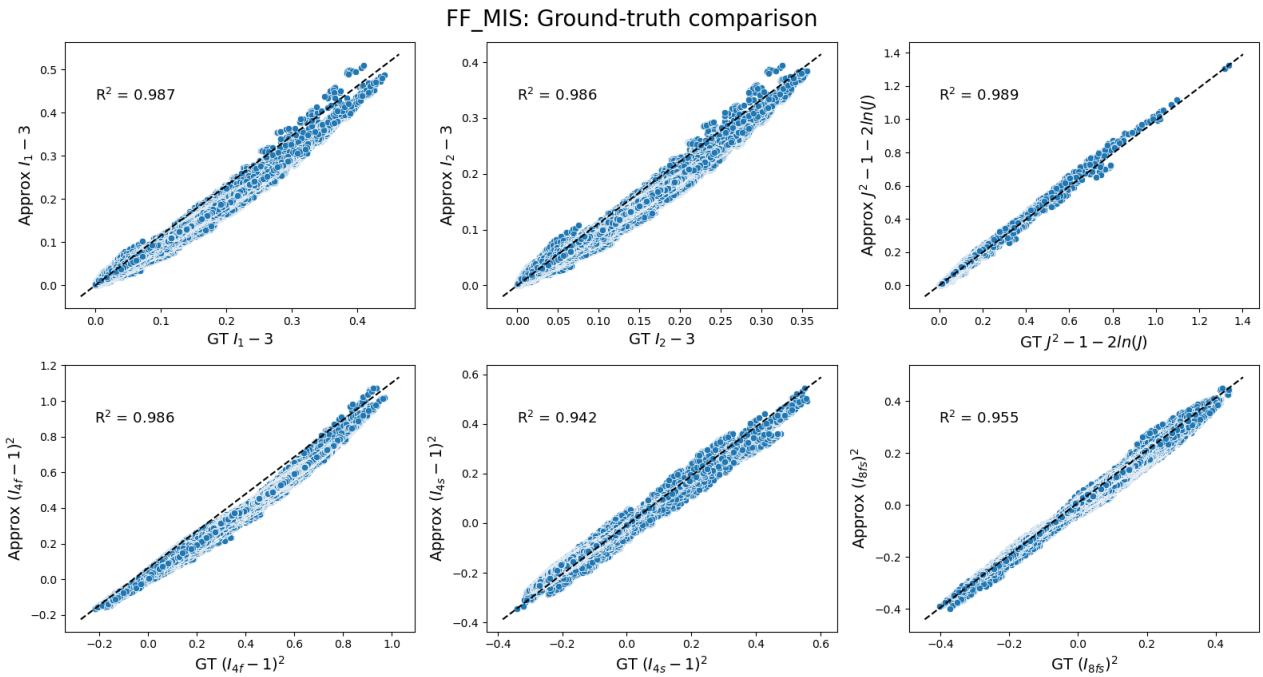

Fig. 21. The energy plots produced by the validation sample after FEM simulation using both the ground truth and the predicted model for the most informative slice. On the top left the $I_1 - 3$ energies are compared, in the top center the $I_2 - 3$ energies are compared, on the top right the volumetric energies are compared, on the bottom left the $I_{4f} - 1$ energies are compared, on the bottom center the $I_{4s} - 1$ energies are compared, and on the bottom right the I_{8fs} energies are compared. All plots have a dashed center line that depicts the ideal relationship between the energies of the ground truth and the approximated model.

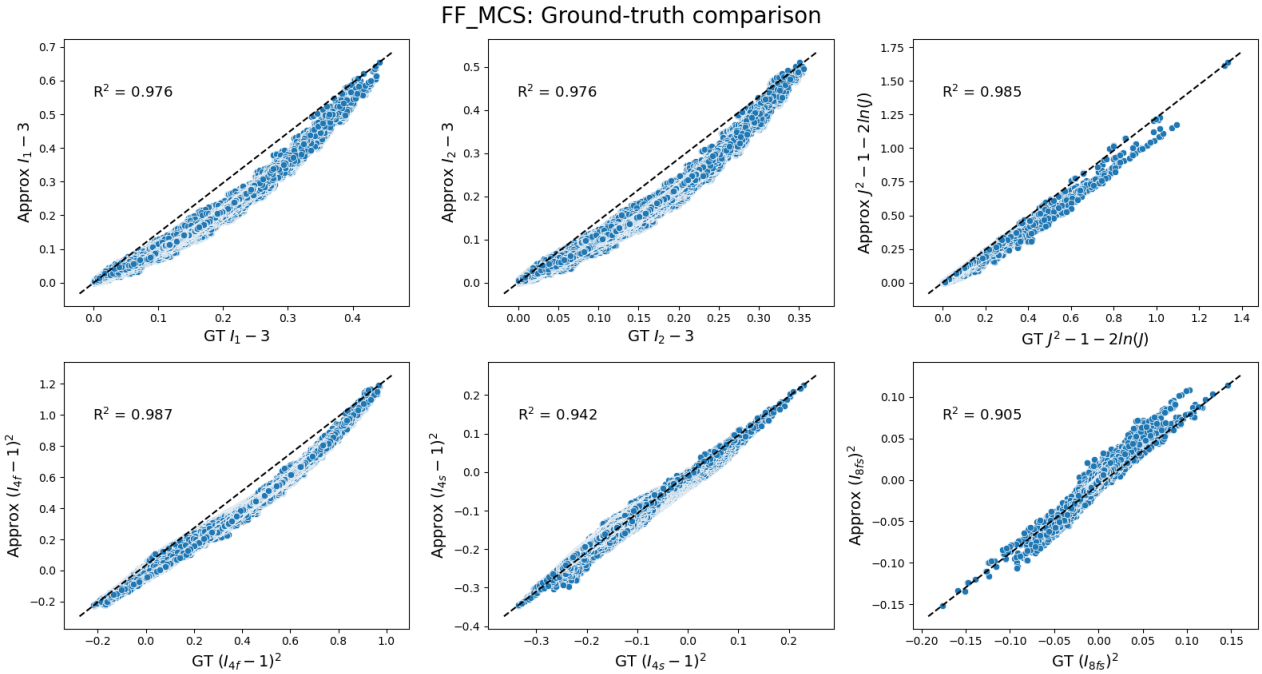

Fig. 22. The energy plots produced by the validation sample after FEM simulation using both the ground truth and the predicted model for the most common slice. On the top left the $I_1 - 3$ energies are compared, in the top center the $I_2 - 3$ energies are compared, on the top right the volumetric energies are compared, on the bottom left the $I_{4f} - 1$ energies are compared, in the bottom center the $I_{4s} - 1$ energies are compared and in the bottom right the I_{8fs} energies are compared. All plots have a dashed center line that depicts the ideal relationship between the energies of the ground truth and the approximated model.

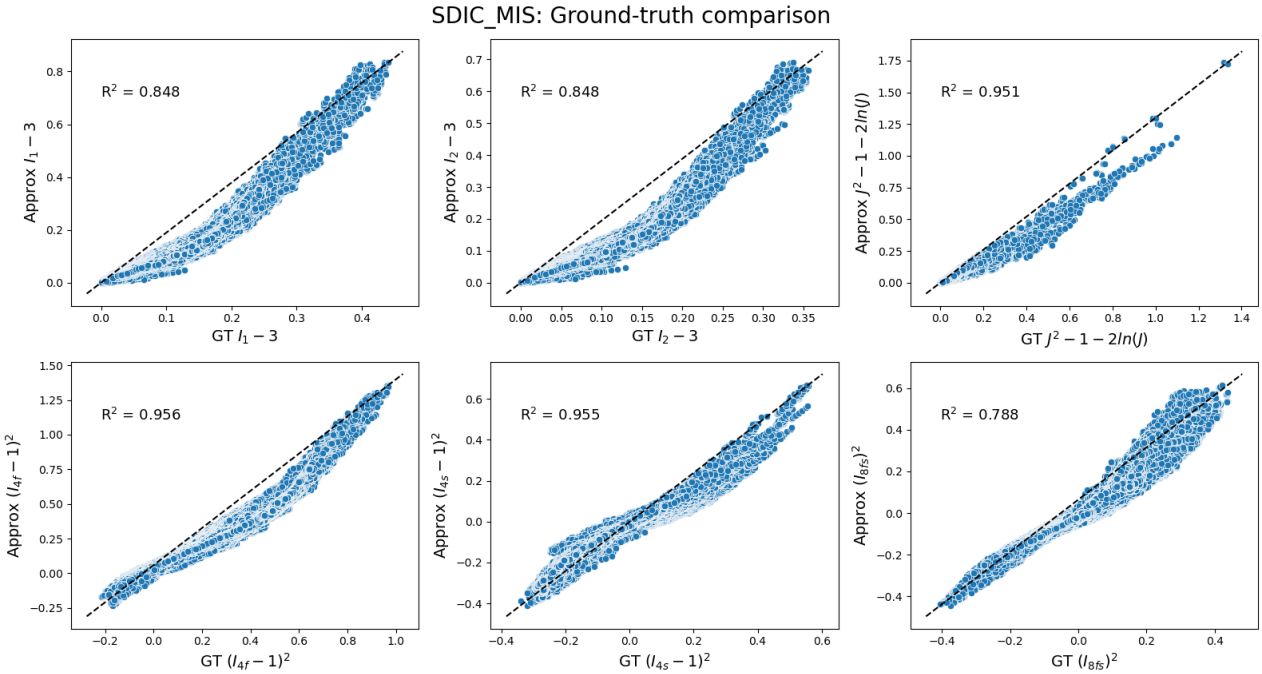

Fig. 23. The energy plots produced by the validation sample after FEM simulation using both the ground truth and the predicted model for the most informative slice when using the stereo DIC field approximation method. On the top left the $I_1 - 3$ energies are compared, in the top center the $I_2 - 3$ energies are compared, on the top right the volumetric energies are compared, in the bottom left the $I_{4f} - 1$ energies are compared, in the bottom center the $I_{4s} - 1$ energies are compared, and in the bottom right the I_{8fs} energies are compared. All plots have a dashed center line that depicts the ideal relationship between the energies of the ground truth and the approximated model.

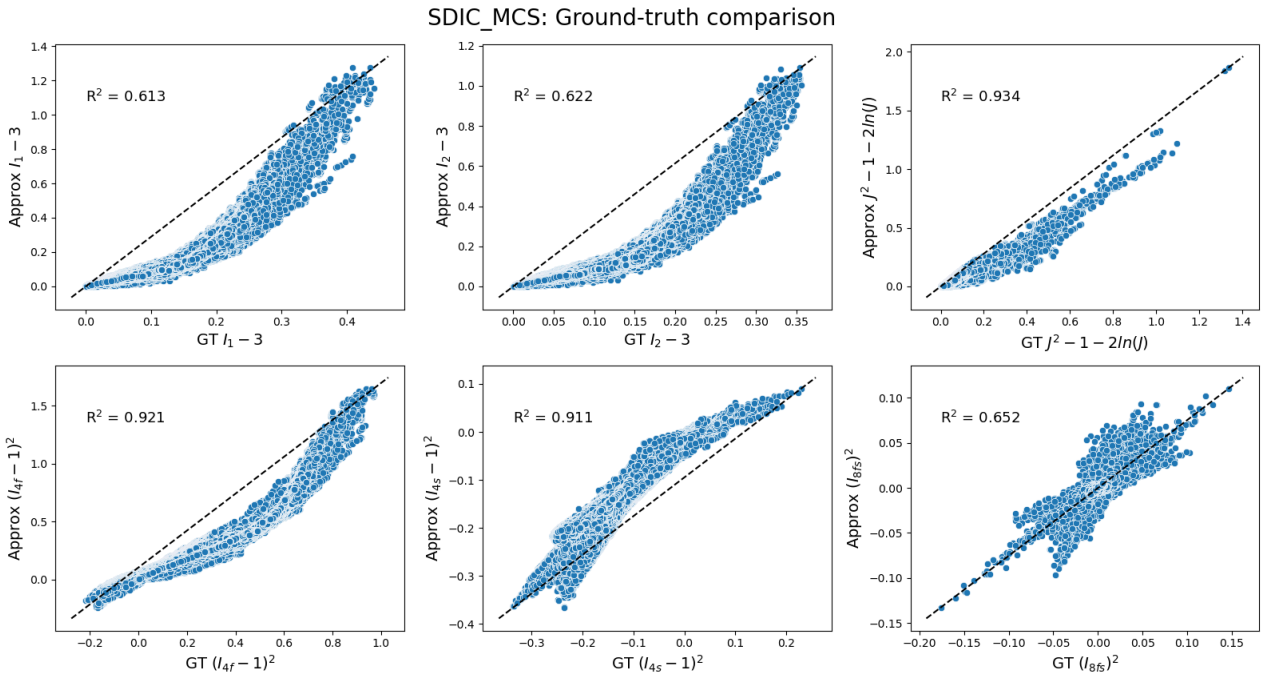

Fig. 24. The energy plots produced by the validation sample after FEM simulation using both the ground truth and the predicted model for the most common slice when using the stereo DIC field approximation method. On the top left the $I_1 - 3$ energies are compared, in the top center the $I_2 - 3$ energies are compared, on the top right the volumetric energies are compared, on the bottom left the $I_{4f} - 1$ energies are compared, in the bottom center the $I_{4s} - 1$ energies are compared, and in the bottom right the I_{8fs} energies are compared. All plots have a dashed center line that depicts the ideal relationship between the energies of the ground truth and the approximated model.

3.C. Validation of the predicted models. To validate the material models, a separate simulation was performed with a new geometry and using a uniaxial tensile test to overcome the symmetrical properties of the simulation. The simulation was performed with five different material models; the ground truth (HO-model), the FF-MIS model, the SDIC-MIS model, the FF-MCS model, and the SDIC-MCS model.

Three types of graphs are considered in this section. One shows the correlation between the ground truth material model and the approximate model for the energies of six core features. These features are: $I_1 - 3$, $I_2 - 3$, $J^2 - 1 - 2ln(J)$, $(I_{4f} - 1)^2$, $(I_{4s} - 1)^2$, $(I_{8fs})^2$. A dashed black line in these graphs indicates the ideal relationship between the two models. Blue dots indicate the energy values for each element in the meshed geometry. Similarly to the approach above, R^2 values are presented to give a quantitative value to the performance of the fit.
The second plot shows the correlation between the energies of the six core features. The energies are calculated for each integration point and for each element. The obtained energies of the validation mesh are shown in orange, and the energies of the training mesh are shown in blue.
The final graph is a bar graph comparing the R^2-scores between the approximate models.

In Figure 21 a scatter plot is presented showing the energies for each integration point and each finite element of the validation model. The compared energies are obtained from a simulation using the ground truth model and the FF-MIS model. The figure shows qualitatively linear relationships between the approximated model and the ground truth model. This indicates that the approximate model represents the ground-truth model, even when applied to a new geometry. This is further indicated by the R^2 values for each graph. These values range from 0.942 to 0.989, quantitatively indicating good correspondence with the ground truth.
Similarly, the results of the FF-MCS model are presented in Figure 22. Qualitatively linear relationships are again found in the energy plots of the features: $J^2 - 1 - 2ln(J)$, $(I_{4f} - 1)^2$, and $(I_{8fs})^2$. The remaining features show slight downward curvatures, indicating that some underlying behavior is missing from the model. The R^2 scores still indicate that relatively good performance is achieved, as these range from 0.905 to 0.987.
Validation against the ground truth for the SDIC-MIS model is shown in Figure 23. Compared to Figure 22, the deviations from the dashed line are greater. That mechanical behavior is missing compared to the ground-truth model becomes more apparent when the R^2 values are considered. These values range from 0.788 to 0.956.
The last model considered in this validation is the SDIC-MCS model which is presented in Figure 24. Large deviations from the dashed line are visible in the graph as the energy plot curves upward, favoring the bottom x-axis. This indicates that the ground-truth model has higher energy values than the approximate model. The performance of the method is also quantified

with the R^2 score, with values ranging from 0.613 to 0.934.

The R^2 scores are more easily compared in Figure 25. In this figure, it becomes clear that the FF-MIS model boasts the highest R^2 score with the least variance in its value. The FF-MCS model shows only slightly lower average values for the R^2 score and also has a slightly larger variance. Compared to the full deformation field models, the models using the SDIC measurements have significantly lower R^2 values and higher variance.

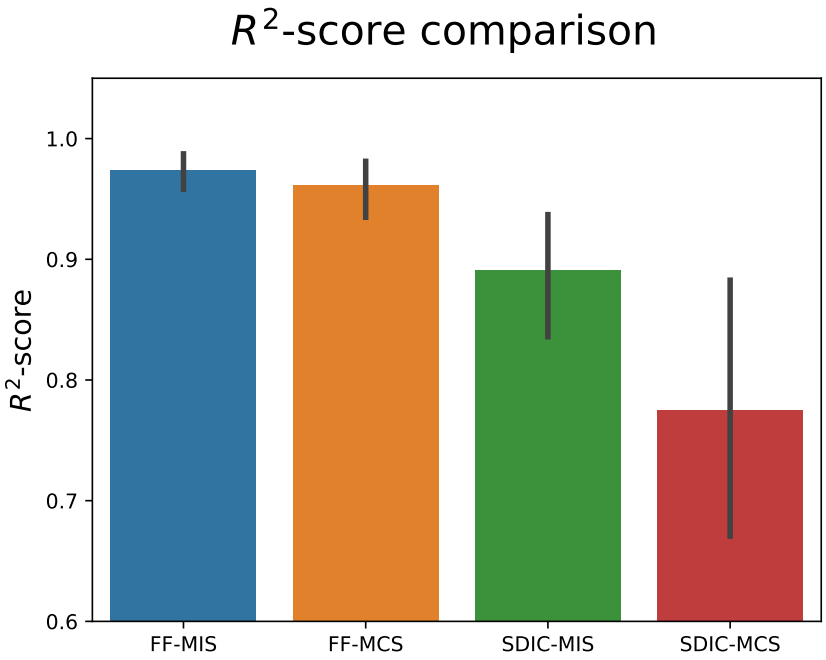

Fig. 25. A bar graph showing the R^2 scores of the four models and their variance. These R^2 scores are the result of comparing the energies in the model with the ground-truth material model.

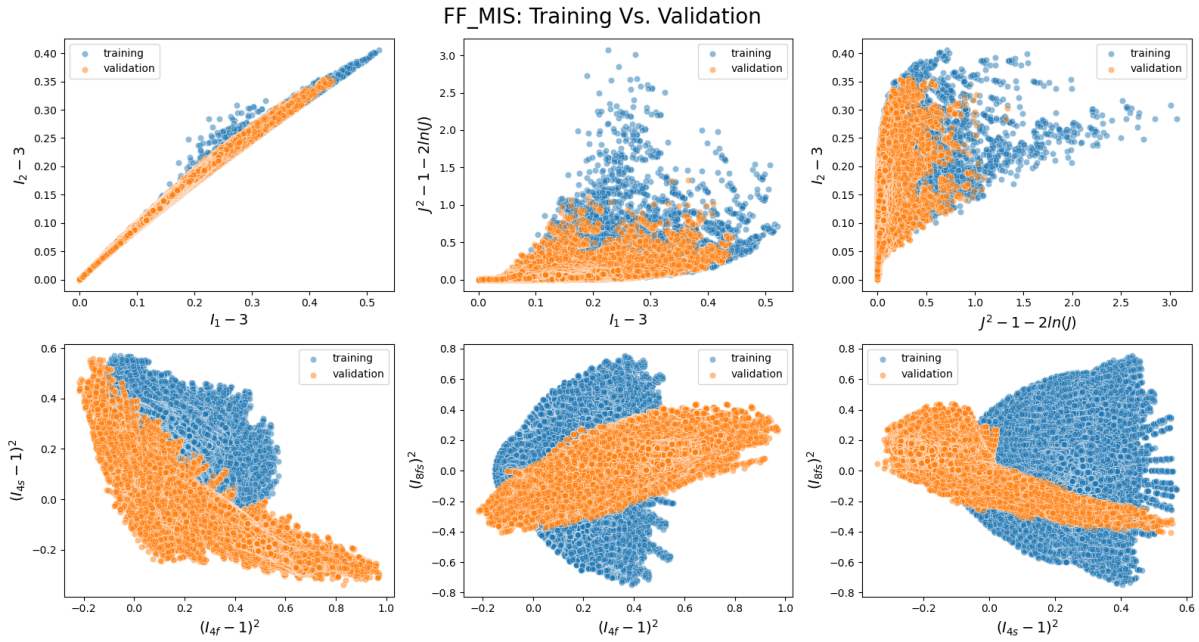

Fig. 26. The energy per finite element of the validation sample, obtained from FEM simulation with the ground truth material model for the most informative slice, was compared to the energy per finite element of the training sample using the most informative slice of the approximated material model. The energies obtained from the training sample are colored blue, whereas the energies in orange correspond to those obtained from the validation sample.

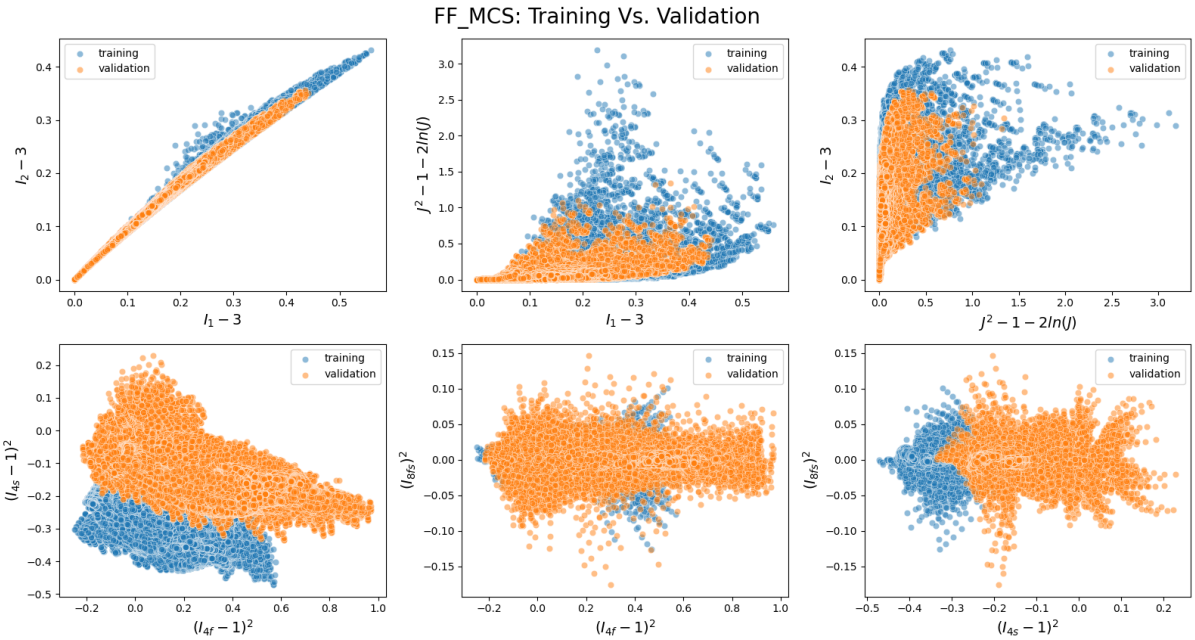

Fig. 27. The energy per finite element of the validation sample, obtained from FEM simulation with the ground truth material model for the most common slice, was compared to the energy per finite element of the training sample with the most common slice of the approximated material model. The energies obtained from the training sample are depicted in blue, whereas the energies in orange correspond to those obtained from the validation sample.

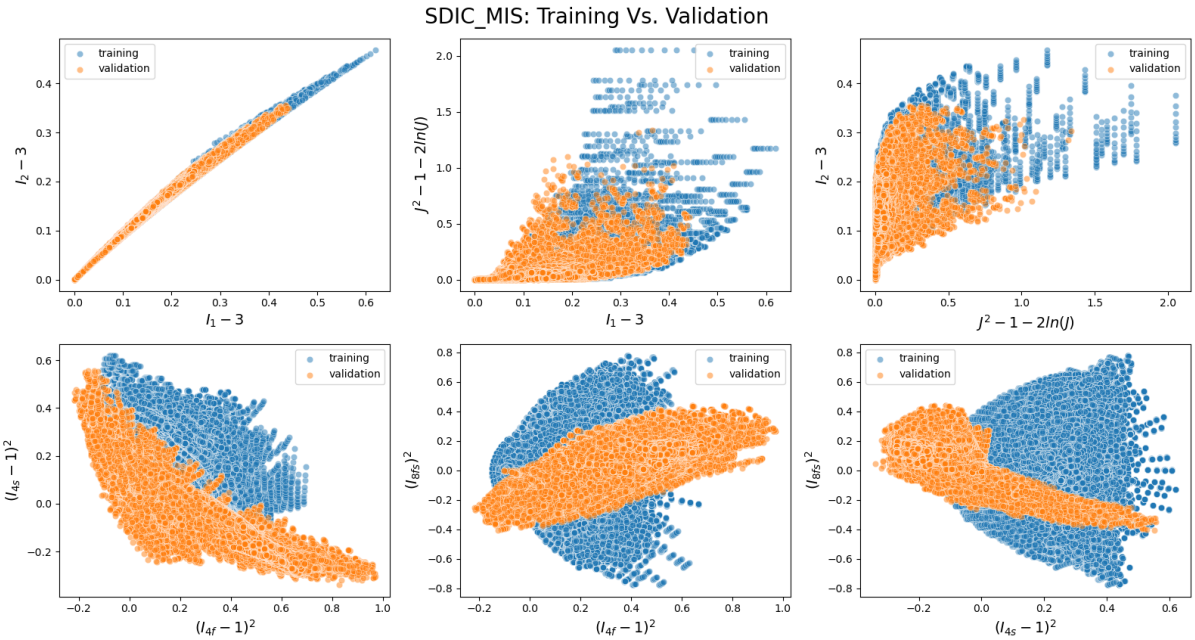

Fig. 28. The energy per finite element of the validation sample, obtained from FEM simulation with the ground truth material model for the most common slice, was compared to the energy per finite element of the training sample with the most common slice of the approximated material model. The energies obtained from the training sample are depicted in blue, whereas the energies in orange correspond to those obtained from the validation sample.

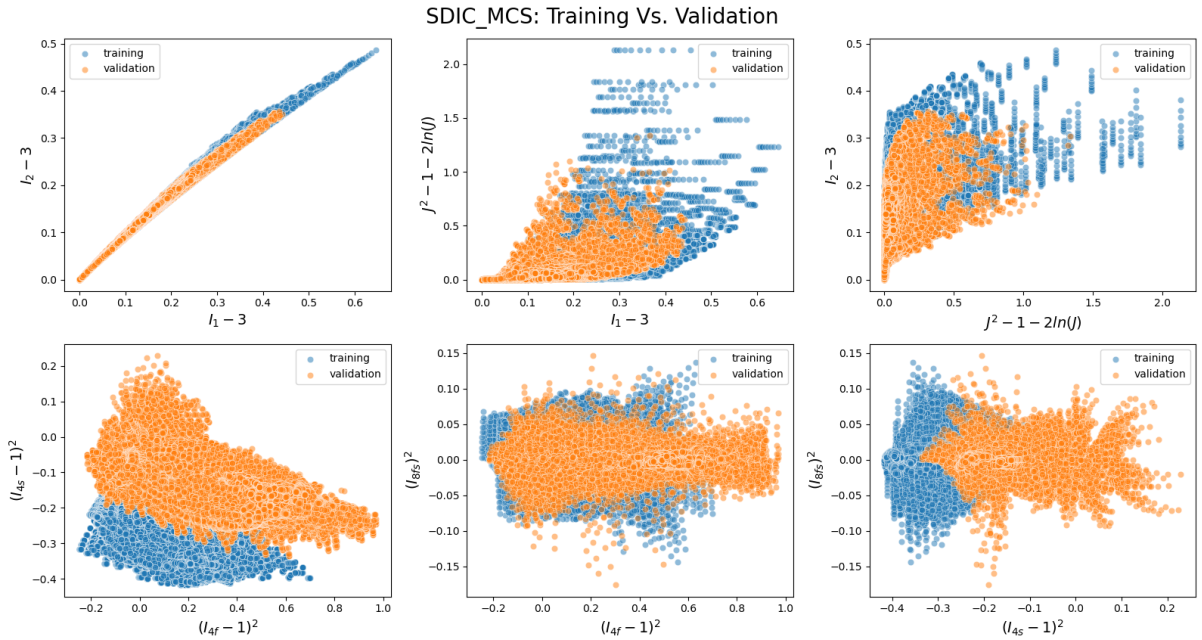

Fig. 29. The energy per finite element of the validation sample, obtained from FEM simulation with the ground truth material model for the most common slice, was compared to the energy per finite element of the training sample with the most common slice of the approximated material model. The energies obtained from the training sample are depicted in blue, whereas the energies in orange correspond to those obtained from the validation sample.

Figures 26, 27, 28, and 29 show the energy per integration point for each element in the training model compared to the validation model. For both of these models, the ground truth material model is used.
All four graphs indicate an overlap between the training and validation data when considering the ($I_1 - 3$, $I_2 - 3$), ($I_1 - 3$, $J^2 - 1 - 2ln(J)$), and ($I_2 - 3$, $J^2 - 1 - 2ln(J)$) plots.
For the remaining plots, however, deviations from the training set are visible. This indicates that the validation data differ mainly in their anisotropic features ($I_{4f} - 1$, $I_{4s} - 1$, and I_{8fs}).
Across all four graphs, the isotropic features are qualitatively comparable. However, differences are found between the anisotropic features when the slicing direction is considered. For example, the ($(I_{4f} - 1)^2$, $(I_{8fs})^2$) plot for the FF-MIS and FF-MCS models differ. The former shows a narrow validation band with a slight upward trajectory, whereas the latter shows an approximately constant horizontal band with a few outliers.

4. Discussion

In this work, I investigated the capability of Bayesian-EUCLID to retrieve a predictive approximate material model for the myocardium in the presence of heterogeneous deformation fields. This capability can be assessed in a few ways;

1. Feature selection: an effective approximation of the material model would contain the same invariants as the ground-truth
2. Quantitative feature identification: the quantitative certainty that the retrieved features are present within the model should be high
3. Predictive capability of the identified model: similar results should be obtained when the identified model and the ground truth are compared in a new geometry with different boundary conditions

Several results and processes are discussed in the following subsections. First, the slicing methods and their corresponding fiber orientations are compared. Second, I discuss the tuning process because it directly influences the obtained results. Third, a comparison between the measurement techniques is discussed. The limitations of this approach are provided next. Finally, the recommendations of this work are given.

4.A. Slicing methods. When looking at the predictive capability of the model obtained from varying slicing directions, it is noteworthy that the eighth invariant feature is discovered only in one instance. Using the most informative slicing direction and the full deformation field, this feature is discovered and the average z activity in Figure 11 is 1, indicating that the method is sure that this feature is present in the ground-truth.
The most common slicing direction, where the sheet fiber points out of the test plane, is at a disadvantage because the sheet fiber direction is not directly pulled upon by the boundary conditions. As a result, the produced model cannot accurately fit the

eighth invariant feature and has difficulty producing $I_{4s} - 1$ feature parameters with high certainty, as indicated by the violin plot in Figure 9.
Previously in the literature, it was determined that a biaxial stretch test is insufficient to characterize the mechanical behavior of the myocardium (under the assumption of homogeneous deformation) (4, 11, 12, 14). In contrast, my results show that with a more advantageously obtained sample and by using heterogeneous deformation fields, the orthotropic and hyperelastic material behavior of the myocardium can be characterized.

When considering the predicted energies along specific deformation paths for the FF-MCS model in Figure 16, large 95 percentile areas are visible in the homogeneous energy plot of the most common slice experiment. During the heuristic hyperparameter fitting process, this was indicative of relatively low values for λ_r, or that the algorithm had otherwise not converged. Further indication that the method had not converged after two iterations is seen in the offset of the mean and true energy curves.

4.B. Hyperparameter tuning. During the heuristic process of tuning the hyperparameter values for the Bayesian-EUCLID algorithm, some specific parameters stand out from the rest. Namely, the chain length N_{links}, the reaction force balance parameter λ_r and the number of degrees of freedom used in the algorithm n_{free}.
The parameter N_{links} denotes how many Gibbs samples are obtained in the MCMC and is therefore influential in the convergence of the method. The chain length was tuned by analyzing the average z-activity. Parsimonious models with average z-activity values close to one for all of the features used are indicative of the convergence of the algorithm. Other indicators are values of R^2 close to 1. If all indicators are present, the algorithm has truly converged. When this is not the case, convergence is not guaranteed. Although the evidence is anecdotal, it was found that if the first indicator was present, but the fit in the energy plot was not satisfactory, increasing λ_r would improve the fit.

Both λ_r and n_{free} are directly related when considering the construction of the matrix $\boldsymbol{A}$ as in equation 39. The conditioning of this matrix is largely influential in the convergence of the method. Therefore, choosing high values of λ_r can quickly make the matrix ill-conditioned. After analyzing the results, the choice of λ_r, if n_{free} is kept constant, depends on the reaction forces and the number of nodes in the model. Furthermore, the optimal values of λ_r seem to depend on the number of features available for discovery, or present within the model. This might indicate that λ_r can be changed when the feature-set is reduced in the second iteration of the algorithm. An improvement on the method might be to use matrix conditioning techniques that automatically scale the importance of the force balance parameter λ_r.

The parameter z_{cutoff} was chosen with an initial guess in mind. The average z-activity symbolizes the occurrence of the feature in the model percentage-wise. As such, choosing a value of 0.5 means that 50% of the models contain such a feature. This was deemed a sufficiently stringent value for this work.
The other hyperparameter values were chosen to be the same as those in the Bayesian-EUCLID paper (22).

4.C. Differences between FF and SDIC models. When considering the features discovered in both data-sets, clearly the models trained on the full deformation field are preferred. The most informative slicing direction performs very well in this case, providing the desired model features and showing R^2 values with an average of 0.974. The FF-MCS experiment was able to detect the sheet fiber direction feature, albeit with a considerable amount of variability as indicated by the violin plot in Figure 15. However, it was unable to retrieve the fiber coupling invariant I_{8fs} from the data.

The resulting SDIC-MIS model contains both $I_{4f} - 1$ and $I_{4s} - 1$ features. Although the eighth invariant is not present in the model, R^2 values in the validation process were reasonably high with an average of 0.891. The fact that this invariant is not recovered from the data correlates with the statement of Holzapfel and Ogden that biaxial stretch testing can only retrieve transversely isotropic material models (4). Although they used the assumption that the sample was undergoing homogeneous deformation, which is not present in this work, the act of approximating the three-dimensional displacement field from top-surface measurements could have filtered out the behavior that makes this material orthotropic. The ground-truth comparison results presented in Figure 24 of the SDIC-MCS model show that only using the $I_{4f} - 1$ feature is insufficient for a predictive model description.

4.D. Limitations. One of the main limitations of this work is the use of a comparably low-value bulk modulus. As a result, the material is allowed to dilate excessively. The reason why such a low value is used in the first place is due to the implementation of the finite element method and its limitations. Because the simulation did not converge for higher values of the bulk modulus and the required amount of Newton-Rhapson iterations progressively increased, it was stipulated that the elements in the simulation were exhibiting overly stiff behavior which could be caused by volumetric locking. The current implementation of the in-house developed Python code does not include sufficiently advanced techniques to deal with these convergence issues.

Literature has shown that compressibility is not negligible in the perfused myocardium (6, 27, 28). The maximum increase in volume was found to range from 2.15% to 6.05%. These values are lower than those found in the results of the finite element analysis which show a distribution ranging from 0% to 50% and centered around 25% with outliers at 110%. These results are presented in Appendix C.

The assumption of incompressibility is often applied in order to facilitate the parameter fitting process by eliminating variables from the constitutive equations. This elimination process is not necessary in this current implementation of the Bayesian-EUCLID method. However, adding an additional volumetric feature that enforces incompressible behavior can allow the method to infer if the myocardium is truly incompressible from experimental data.

A short exploratory look into the literature revealed that more care must be taken when simulating compressibility in anisotropic materials. Non-physical results could arise when anisotropic materials are simulated due to the deviatoric and isochoric split of the SEDF (29, 30). Some techniques presented in these studies show how to circumvent these non-physical results.

Within the scope of this work, we assumed that the myocardium behaves in a hyperelastic and orthotropic manner. For a better reconstruction of the mechanical test data using FEM, other behavioral effects such as viscoelasticity and plasticity should also be considered, as the effects of hysteresis were clearly present in the experimental results of the biaxial stretch and triaxial shear tests (11, 12).

Due to the exploratory nature of this study, no hyperparameter fitting study has been performed within it. Therefore, the hyperparameter values provided within this work will not reflect optimal choices of such parameter values. Replication of this study with different materials and geometries requires a new set of hyperparameters to obtain accurate results.

4.E. Recommendations.

E.1. Improvements on the method. As a result of the limitations the most pertinent recommendation we can make is to address the issue of compressibility with anisotropic materials. Making use of industry-standard software, such as ABAQUS might prove useful in this pursuit, but an amicable implementation of hybrid elements or selectively reduced integration techniques within the current software might prove just as valuable. Furthermore, considerations of the non-physical results due to the isochoric and deviatoric split can also aid the performance of the method (29, 30).

The current implementation of the Bayesian-EUCLID method requires a priori knowledge of the fiber orientations in the sample to fit a constitutive model to the data. If this method were to be extended so that it could also predict the fiber orientation, it would prove to be an invaluable method for identifying constitutive models with uncertainty quantification.

The most informative slicing direction was chosen to provide an upper bound to the discoverability of the material model. A better approximation of reality considers a heterogeneous dispersion of the fibers throughout the material. A next step for this study would be to simulate such a sample and to test the ability of Bayesian-EUCLID to retrieve the orthotropic and hyperelastic material model. A sensitivity study could show the dependence on the fiber distribution throughout the material.

Effects such as viscoelasticity and plasticity have been left outside of the scope of this study. Including these effects in the simulation and adapting the EUCLID method to address such behavior is another big step in taking this research further.

Hyperparameter λ_r has a large influence on the predictive capacity of the model. This is due to its influence on the conditioning of the matrix in equation 39. Increasing the condition number will improve the influence of the reaction forces on the final result, but will decrease the chance the algorithm has to converge to a solution. A matrix conditioning method which allows for an optimal reaction force balance is therefore beneficial for this Bayesian-EUCLID method.

E.2. Comparison between current testing methods. Triaxial shear testing is currently considered a requirement for the characterization of the myocardium (4, 11, 12). The testing method requires the gluing of samples onto testing plates, which might chemically and mechanically influence the constitutive behavior of the material. Compare this with the biaxial stretch test, where this is not required. Sutures or rakes are used to fix the material in place and provide Dirichlet boundary conditions. However, this might introduce heterogeneity in the deformation field (14). This heterogeneity of the deformation field might be similar to the one induced in this study.

Because the FF-MIS model shows good predictive capabilities, it can be argued that the biaxial stretch test is sufficiently advanced to characterize the mechanical behavior of the myocardium in the presence of a heterogeneous deformation field. When the material is characterized through a biaxial stretch test, it is imperative that the full displacement field is measured and an optimal fiber distribution, such as the most informative slicing direction considered in this work, is used.

5. Conclusion

The results of this exploratory study show that the constitutive behavior of the myocardium can be characterized from biaxial stretch test measurements that exhibit heterogeneous deformations using the Bayesian-EUCLID method. Full displacement field measurements allow the method to identify all invariant features of the HO-model (which serves as a ground-truth material model in this study) when applied to a sample with an optimal fiber distribution within the plane of the biaxial stretch test. The validation process of this material model shows good correspondence with the ground truth through an average R^2 value of 0.974. The SDIC measurements produce data-sets which allow the Bayesian-EUCLID method to identify material models with two distinct fiber contributions. When the direction of the sheet fiber does not lie within the plane of the biaxial stretch test, the resulting material model cannot describe the orthotropic nature of the myocardium.

Future perspectives of this study include adapting the Bayesian-EUCLID method to more complex behaviors such as viscoelasticity and plasticity to determine even more realistic model predictions for the myocardium. Another future improvement includes the addition of heterogeneously dispersed fibers in the simulation and the ability for the Bayesian-EUCLID method to use these to its advantage.

ACKNOWLEDGEMENTS

I would like to thank my supervisors M. Peirlinck and S. Kumar for their guidance and thought-provoking conversations. My thanks also go out to my colleagues S. Cardona, L. Maga and B. Moscoloni for their invaluable input and support. I would also like to thank my friends and family for their love and support. Special thanks to M. Rood and M. Brands for their capacity to endure my unending ramblings about my thesis.

Bibliography

1. Sabina Andreea Leancă, Daniela Crișu, Antoniu Octavian Petriș, Irina Afrăsânie, Antonia Genes, Alexandru Dan Costache, Dan Nicolae Tesloianu, and Irina Iuliana Costache. Left Ventricular Remodeling after Myocardial Infarction: From Physiopathology to Treatment. *Life*, 12(8):1111, July 2022. ISSN 2075-1729. doi: 10.3390/life12081111.
2. Dirk Westermann, Mario Kasner, Paul Steendijk, Frank Spillmann, Alexander Riad, Kerstin Weitmann, Wolfgang Hoffmann, Wolfgang Poller, Matthias Pauschinger, Heinz-Peter Schultheiss, and Carsten Tschöpe. Role of left ventricular stiffness in heart failure with normal ejection fraction. *Circulation*, 117(16):2051–2060, April 2008. ISSN 1524-4539. doi: 10.1161/CIRCULATIONAHA.107.716886.
3. Ramona Emig, Callum M. Zgierski-Johnston, Viviane Timmermann, Andrew J. Taberner, Martyn P. Nash, Peter Kohl, and Rémi Peyronnet. Passive myocardial mechanical properties: meaning, measurement, models. *Biophysical Reviews*, 13(5):587–610, October 2021. ISSN 1867-2450. doi: 10.1007/s12551-021-00838-1.
4. Gerhard A. Holzapfel and Ray W. Ogden. Constitutive modelling of passive myocardium: a structurally based framework for material characterization. *Philosophical Transactions of the Royal Society A: Mathematical, Physical and Engineering Sciences*, 367(1902):3445–3475, September 2009. ISSN 1364-503X, 1471-2962. doi: 10.1098/rsta.2009.0091.
5. K. D. Costa, J. W. Holmes, and A. D. Mcculloch. Modelling cardiac mechanical properties in three dimensions. *Philosophical Transactions of the Royal Society of London. Series A: Mathematical, Physical and Engineering Sciences*, 359(1783):1233–1250, June 2001. ISSN 1364-503X, 1471-2962. doi: 10.1098/rsta.2001.0828.
6. F. Barış Can Cansız, Hüsnü Dal, and Michael Kaliske. An orthotropic viscoelastic material model for passive myocardium: theory and algorithmic treatment. *Computer Methods in Biomechanics and Biomedical Engineering*, 18(11):1160–1172, August 2015. ISSN 1025-5842. doi: 10.1080/10255842.2014.881475. Publisher: Taylor & Francis _eprint: https://doi.org/10.1080/10255842.2014.881475.
7. Osman Gültekin, Gerhard Sommer, and Gerhard A. Holzapfel. An orthotropic viscoelastic model for the passive myocardium: continuum basis and numerical treatment. *Computer Methods in Biomechanics and Biomedical Engineering*, 19(15):1647–1664, November 2016. ISSN 1025-5842. doi: 10.1080/10255842.2016.1176155. Publisher: Taylor & Francis _eprint: https://doi.org/10.1080/10255842.2016.1176155.
8. Reza Avazmohammadi, João S. Soares, David S. Li, Samarth S. Raut, Robert C. Gorman, and Michael S. Sacks. A Contemporary Look at Biomechanical Models of Myocardium. *Annual Review of Biomedical Engineering*, 21:417–442, June 2019. ISSN 1545-4274. doi: 10.1146/annurev-bioeng-062117-121129.
9. Deboa Guan, Faizan Ahmad, Peter Theobald, Shwe Soe, Luo, and Gao. On the AIC-based model reduction for the general Holzapfel–Ogden myocardial constitutive law - PMC, November 2018.
10. Sotirios Kakaletsis, William D. Meador, Mrudang Mathur, Gabriella P. Sugerman, Tomasz Jazwiec, Marcin Malinowski, Emma Lejeune, Tomasz A. Timek, and Manuel K. Rausch. Right ventricular myocardial mechanics: Multi-modal deformation, microstructure, modeling, and comparison to the left ventricle. *Acta Biomaterialia*, 123:154–166, March 2021. ISSN 1742-7061. doi: 10.1016/j.actbio.2020.12.006.
11. Dokos. Shear properties of passive ventricular myocardium, 2002.
12. Gerhard Sommer, Andreas J. Schriefl, Michaela Andrä, Michael Sacherer, Christian Viertler, Heimo Wolinski, and Gerhard A. Holzapfel. Biomechanical properties and microstructure of human ventricular myocardium. *Acta Biomaterialia*, 24:172–192, September 2015. ISSN 1742-7061. doi: 10.1016/j.actbio.2015.06.031.
13. Reza Avazmohammadi, David S. Li, Thomas Leahy, Elizabeth Shih, João S. Soares, Joseph H. Gorman, Robert C. Gorman, and Michael S. Sacks. An integrated inverse model-experimental approach to determine soft tissue three-dimensional constitutive parameters: application to post-infarcted myocardium. *Biomechanics and Modeling in Mechanobiology*, 17(1):31–53, February 2018. ISSN 1617-7940. doi: 10.1007/s10237-017-0943-1.
14. Heleen Fehervary, Marija Smoljkić, Jos Vander Sloten, and Nele Famaey. *Planar biaxial testing of soft biological tissues*. PhD thesis, August 2018.
15. Prabhakar Shantha Rajiah, Kevin Kalisz, Jordi Broncano, Harold Goerne, Jeremy D. Collins, Christopher J. François, El-Sayed Ibrahim, and Prachi P. Agarwal. Myocardial Strain Evaluation with Cardiovascular MRI: Physics, Principles, and Clinical Applications. *RadioGraphics*, 42(4):968–990, July 2022. ISSN 0271-5333. doi: 10.1148/rg.210174. Publisher: Radiological Society of North America.
16. Michael S. Sacks. Biaxial Mechanical Evaluation of Planar Biological Materials. *Journal of elasticity and the physical science of solids*, 61(1):199–246, July 2000. ISSN 1573-2681. doi: 10.1023/A:1010917028671.
17. Kailai Xu, Daniel Z. Huang, and Eric Darve. Learning Constitutive Relations using Symmetric Positive Definite Neural Networks, April 2020. arXiv:2004.00265 [cs, math].
18. Daniel Z. Huang, Kailai Xu, Charbel Farhat, and Eric Darve. Learning constitutive relations from indirect observations using deep neural networks. *Journal of Computational Physics*, 416:109491, September 2020. doi: 10.1016/j.jcp.2020.109491. MAG ID: 3022973855.
19. Huaiqian You, Quinn Zhang, Colton J. Ross, Chung-Hao Lee, Ming-Chen Hsu, and Yue Yu. A Physics-Guided Neural Operator Learning Approach to Model Biological Tissues From Digital Image Correlation Measurements. *Journal of Biomechanical Engineering*, 144(12), October 2022. ISSN 0148-0731. doi: 10.1115/1.4055918.
20. K. Linka and E. Kuhl. A new family of Constitutive Artificial Neural Networks towards automated model discovery. *Computer Methods in Applied Mechanics and Engineering*, 403, 2023. ISSN 0045-7825. doi: 10.1016/j.cma.2022.115731.
21. Moritz Flaschel, Siddhant Kumar, and Laura De Lorenzis. Unsupervised discovery of interpretable hyperelastic constitutive laws. *Computer Methods in Applied Mechanics and Engineering*, 381:113852, 2021. ISSN 00457825. doi: 10.1016/j.cma.2021.113852. arXiv: 2010.13496 Publisher: Elsevier B.V.
22. Akshay Joshi, Prakash Thakolkaran, Yiwen Zheng, Maxime Escande, Moritz Flaschel, Laura De Lorenzis, and Siddhant Kumar. Bayesian-EUCLID: Discovering hyperelastic material laws with uncertainties. *Computer Methods in Applied Mechanics and Engineering*, 398:115225, 2022. ISSN 00457825. doi: 10.1016/j.cma.2022.115225. arXiv: 2203.07422 Publisher: Elsevier B.V.
23. J. C. Zhu, M. Ben Bettaieb, and F. Abed-Meraim. Comparative study of three techniques for the computation of the macroscopic tangent moduli by periodic homogenization scheme. *Engineering with Computers*, 38(2):1365–1394, April 2022. ISSN 0177-0667, 1435-5663. doi: 10.1007/s00366-020-01091-y.
24. Damien Rohmer, Arkadiusz Sitek, and Grant T. Gullberg. Reconstruction and Visualization of Fiber and Laminar Structure in the Normal Human Heart from Ex Vivo Diffusion Tensor Magnetic Resonance Imaging (DTMRI) Data. *Investigative Radiology*, 42(11):777, November 2007. ISSN 0020-9996. doi: 10.1097/RLI.0b013e3181238330.
25. Mathias Peirlinck, Kevin L. Sack, Pieter De Backer, Pedro Morais, Patrick Segers, Thomas Franz, and Matthieu De Beule. Kinematic boundary conditions substantially impact in silico ventricular function. *International Journal for Numerical Methods in Biomedical Engineering*, 35(1):e3151, 2019. ISSN 2040-7947. doi: 10.1002/cnm.3151. _eprint: https://onlinelibrary.wiley.com/doi/pdf/10.1002/cnm.3151.
26. R. Nayek, R. Fuentes, K. Worden, and E. J. Cross. On spike-and-slab priors for Bayesian equation discovery of nonlinear dynamical systems via sparse linear regression. *Mechanical Systems and Signal Processing*, 161:107986, December 2021. ISSN 0888-3270. doi: 10.1016/j.ymssp.2021.107986.
27. F. C. Yin, C. C. Chan, and R. M. Judd. Compressibility of perfused passive myocardium. *American Journal of Physiology-Heart and Circulatory Physiology*, 271(5):H1864–H1870, November 1996. ISSN 0363-6135. doi: 10.1152/ajpheart.1996.271.5.H1864. Publisher: American Physiological Society.

28. Eoin McEvoy, Gerhard A. Holzapfel, and Patrick McGarry. Compressibility and Anisotropy of the Ventricular Myocardium: Experimental Analysis and Microstructural Modeling. *Journal of Biomechanical Engineering*, 140(8), May 2018. ISSN 0148-0731. doi: 10.1115/1.4039947.
29. J. Helfenstein, M. Jabareen, E. Mazza, and S. Govindjee. On non-physical response in models for fiber-reinforced hyperelastic materials. *International Journal of Solids and Structures*, 47(16): 2056–2061, August 2010. ISSN 0020-7683. doi: 10.1016/j.ijsolstr.2010.04.005.
30. Luigi Vergori, Michel Destrade, Patrick McGarry, and Ray W. Ogden. On anisotropic elasticity and questions concerning its Finite Element implementation. *Computational Mechanics*, 52(5): 1185–1197, November 2013. ISSN 1432-0924. doi: 10.1007/s00466-013-0871-6.

Appendices

A. Mesh convergence

Mesh convergence is carried out by selecting points in the geometry of the training sample and subsequently recording the corresponding deformation of these points for varying mesh element sizes. The difference in displacements between the finest mesh sizes and the larger mesh sizes is recorded as an error metric. These errors are plotted in figure 30 for each of their x, y and z components. For clarity, an average error is also shown in the figure. In this graph, we can see that the error in displacements is never greater than 1×10^{-3}, which was deemed sufficient for the purposes of this work.

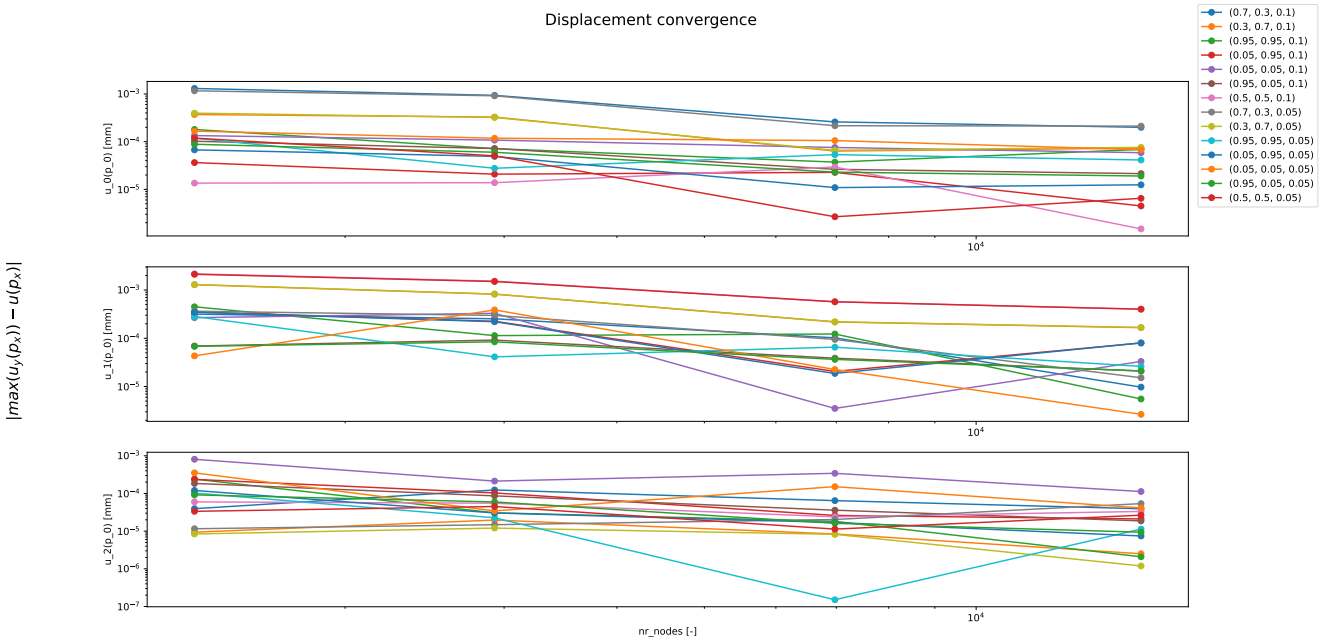

Fig. 30. Mesh convergence plot showing the error between the nodal coordinates of fourteen points on the mesh compared to a mesh with 30380 elements. As the trend of the error slows down the mesh convergences to its solution.

B. hyperparameters

We allow for arbitrary fiber directions within our code by using two basis vectors $\boldsymbol{f}_{base} = \{1,0,0\}$ and $\boldsymbol{s}_{base} = \{0,0,-1\}$ and rotating the set using a Z1-X-Z2 rotation matrix set. The rotation matrices are defined as,

$$\boldsymbol{R}^{Z1} = \begin{bmatrix} cos(\alpha) & -sin(\alpha) & 0 \\ sin(\alpha) & cos(\alpha) & 0 \\ 0 & 0 & 1 \end{bmatrix} \tag{46}$$

$$\boldsymbol{R}^{X} = \begin{bmatrix} 1 & 0 & 0 \\ 0 & cos(\beta) & -sin(\beta) \\ 0 & sin(\beta) & cos(\beta) \end{bmatrix} \tag{47}$$

$$\boldsymbol{R}^{Z2} = \begin{bmatrix} cos(\gamma) & -sin(\gamma) & 0 \\ sin(\gamma) & cos(\gamma) & 0 \\ 0 & 0 & 1 \end{bmatrix} \tag{48}$$

$$\boldsymbol{f} = \boldsymbol{R}^{Z1}\boldsymbol{R}^{X}\boldsymbol{R}^{Z2}\boldsymbol{f}_{base} \tag{49}$$

$$\boldsymbol{s} = \boldsymbol{R}^{Z1}\boldsymbol{R}^{X}\boldsymbol{R}^{Z2}\boldsymbol{s}_{base} \tag{50}$$

Table 1. Summary of parameters used for data generation and identification via Bayesian-EUCLID. MIS stands for Most Informative Slice, MCS stands for Most Common Slice, VGT stands for the validation ground truth which is specifically used to denote the fiber orientations in the material model used in the validation simulation.

Parameter	Notation	Value
Material model:		
rotation in Z1	$[\alpha_{MIS}, \alpha_{MCS}, \alpha_{VGT}]$	$[0.0°, 90.0°, 0.0°]$
rotation in X	$[\beta_{MIS}, \beta_{MCS}, \beta_{VGT}]$	$[-90.0°, 0.0°, -90.0°]$
rotation in Z2	$[\gamma_{MIS}, \gamma_{MCS}, \gamma_{VGT}]$	$[90.0°, 0.0°, 60.0°]$
Bulk modulus	K	1500
Primary stiffness parameter	a	$94.3Pa$
Exponential stiffness parameter	b	5.874
Primary fiber stiffness parameter	a_f	$311.0Pa$
Exponential fiber stiffness parameter	b_f	11.271
Primary sheet fiber stiffness parameter	a_s	$43.1Pa$
Exponential sheet fiber stiffness parameter	b_s	9.772
Primary fiber coupling stiffness parameter	a_{fs}	$25.4Pa$
Exponential fiber coupling stiffness parameter	b_{fs}	2.405
Data generation:		
Number of nodes in mesh	-	15,228
Number of timesteps	L_{static}	10
Number of snapshots	n_t	10
Number of reaction force constraints	n_β	5
Loading parameter in y-direction	ϕ_y	$\{0.03 \times l : l = 1, ..., L_{static}\}$
Loading parameter in x-direction	ϕ_x	$\{0.02 \times l : l = 1, ..., L_{static}\}$
Number of approximant layers	N_L	4
Bayesian learning:		
amplitude of displacement noise	-	1e-012
percentage of the output used	-	0.5
Cutoff value of the average z activity	z_{cutoff}	0.3
Number of feature selection iterations	-	2
Number of free degrees of freedom randomly sampled per snapshot	n_{free}	500
weight parameter of reaction force balance	λ_r	1e-02
Hyperparameters for random variable v_s	(a_v, b_v)	$(0.5, 0.5)$
Hyperparameters for random variable p_0	(a_p, b_p)	$(0.1, 0.5)$
Hyperparameters for random variable σ^2	(a_σ, b_σ)	$(1.0, 1.0)$
Chain length	N_{links}	1000
Numbers of chain links to be burned	N_{burn}	250
Number of parallel chains	N_{chains}	4
Feature library:		
Number of features in library	n_f	24
Number of Mooney-Rivlin features	N_{MR}	4
Number of volumetric features	N_{vol}	1
Highest degree among anisotropic polynomial features	N_{aniso}	4

C. Dilatation results of the simulation

Here, I present the simulation results of the biaxial stretch test using the most informative slicing direction and the ground-truth material model. The deformed geometry showing the values of the dilatation component, or Jacobian, J are shown in Figure 31. The distribution of the average values is shown on the right. This shows that on average the dilatation component is around 1.25, which corresponds to an increase of around 25% in volume.

Figure 32 shows the increase in volume through the dilatation component for the validation geometry. The simulation made use of the ground truth material model. It is notable that the change in volume varies from the previously mentioned results. Here, the dilatation component ranges from 0.96 to 1.4 with outliers up to 1.7.

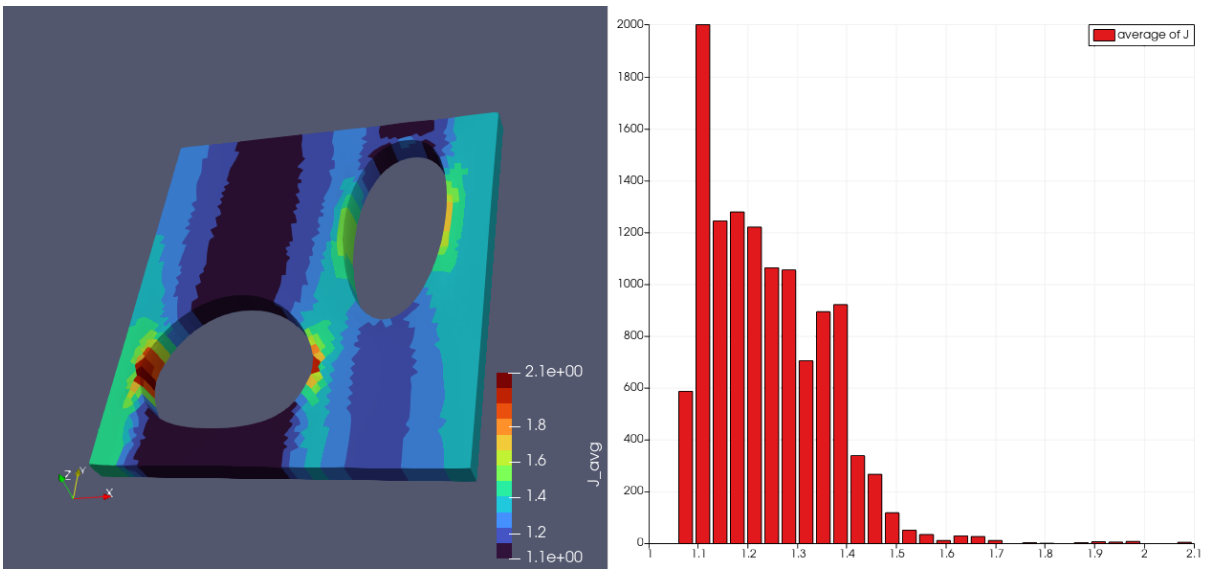

Fig. 31. The plot showing the average dilatation component of each element. The values range from 1.0 to 2.1. The main distribution of these values falls around 1.25.

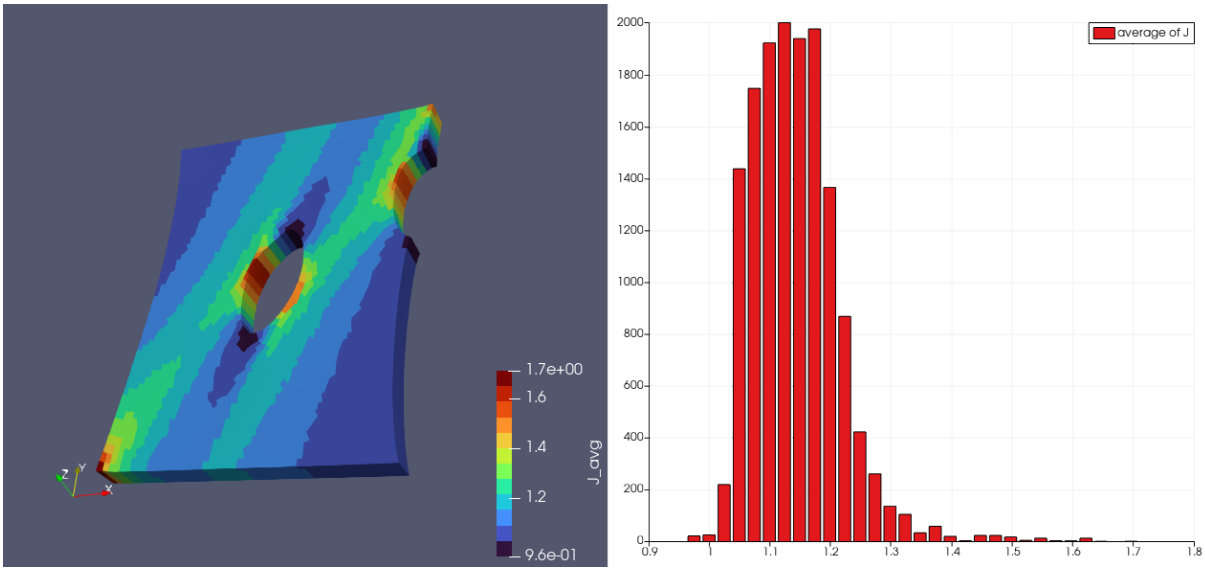

Fig. 32. The plot showing the average dilatation component of each element for the validation geometry and the ground truth material model. The values range from 0.96 to 1.7. The main distribution of these values falls around 1.25.

D. Preliminary results: Uniaxial test results for full-field and most informative slice

In Figure 33 the uniaxially deformed training geometry is shown. For this simulation the most informative slicing direction is used.

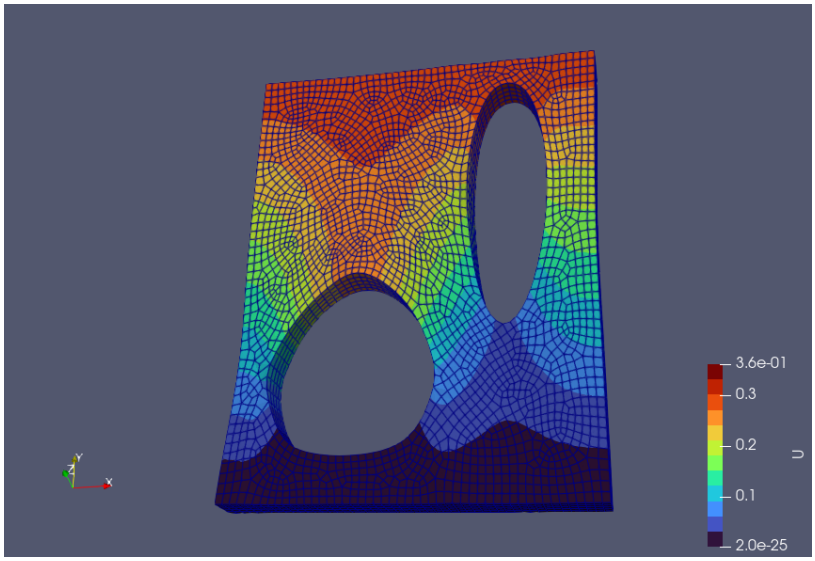

Fig. 33. Mesh of the training sample undergoing uniaxial stretch testing. Note the heterogeneous deformation patters forming around the topside of the bottom left hole and the bottom of the right hole.

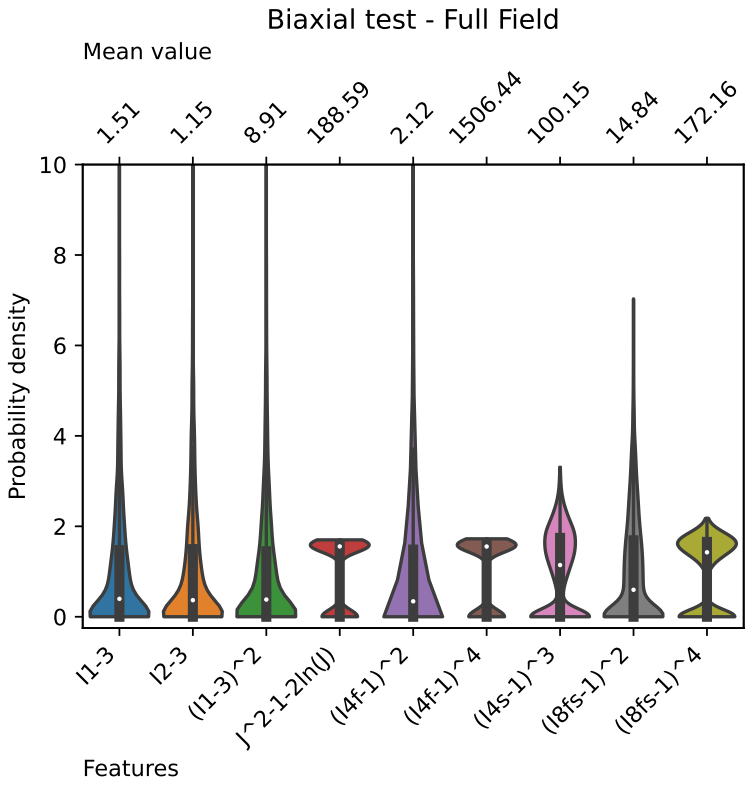

Fig. 34. Violin plot of the most common slice and its discovered features when considering the full deformation field of a uniaxially stretched sample.

The violin plot in Figure 34 shows that Bayesian-EUCLID is able to find an orthotropic material model from the data. From the multimodal distributions within the plot it is noted that the mathod has not yet converged to an optimal solution.

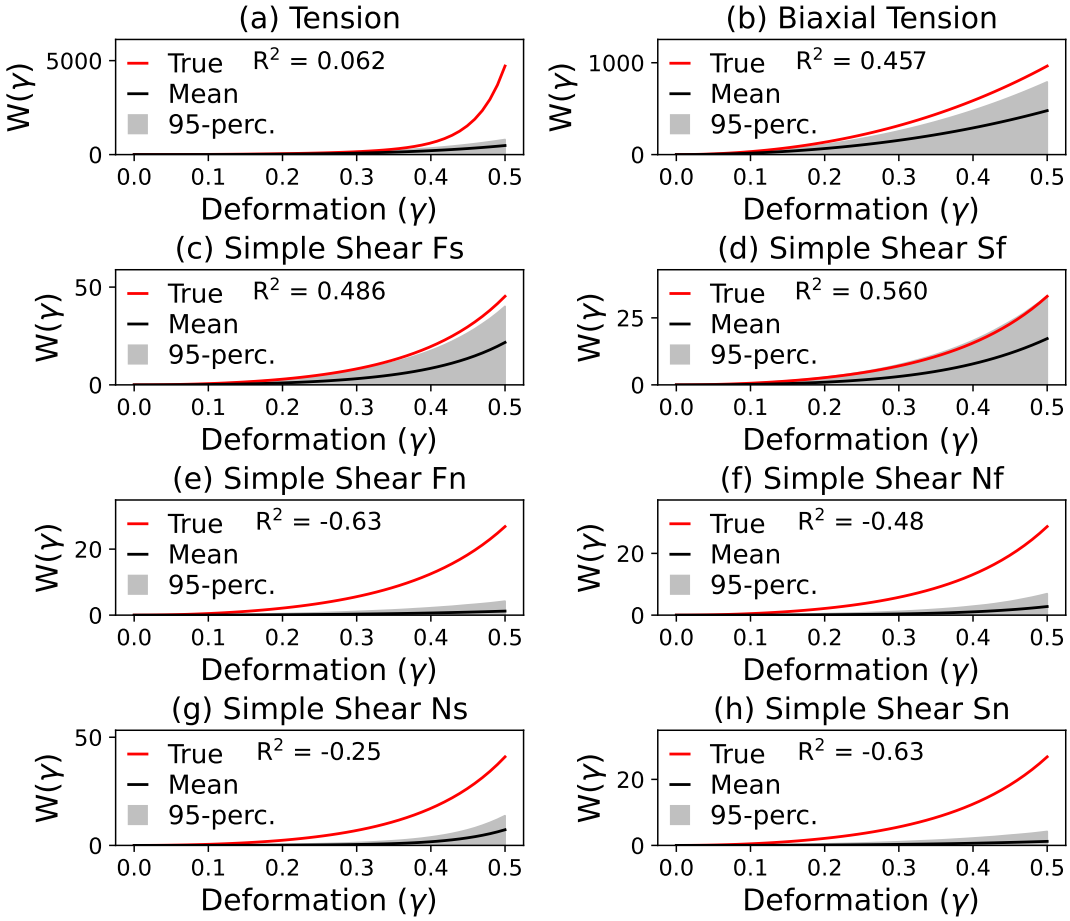

Fig. 35. The ground truth energies compared to the predicted model energies due to imposed deformation gradients when considering the full deformation field, the most informative slice, and a uniaxially stretched sample.

That the method has produced multimodal results with a high certainty that the parameter values might be zero is especially prevalent in Figure 35. In this figure it is noticable that the 95 percentile varies widely. The corresponding R^2-values are also considerably low.

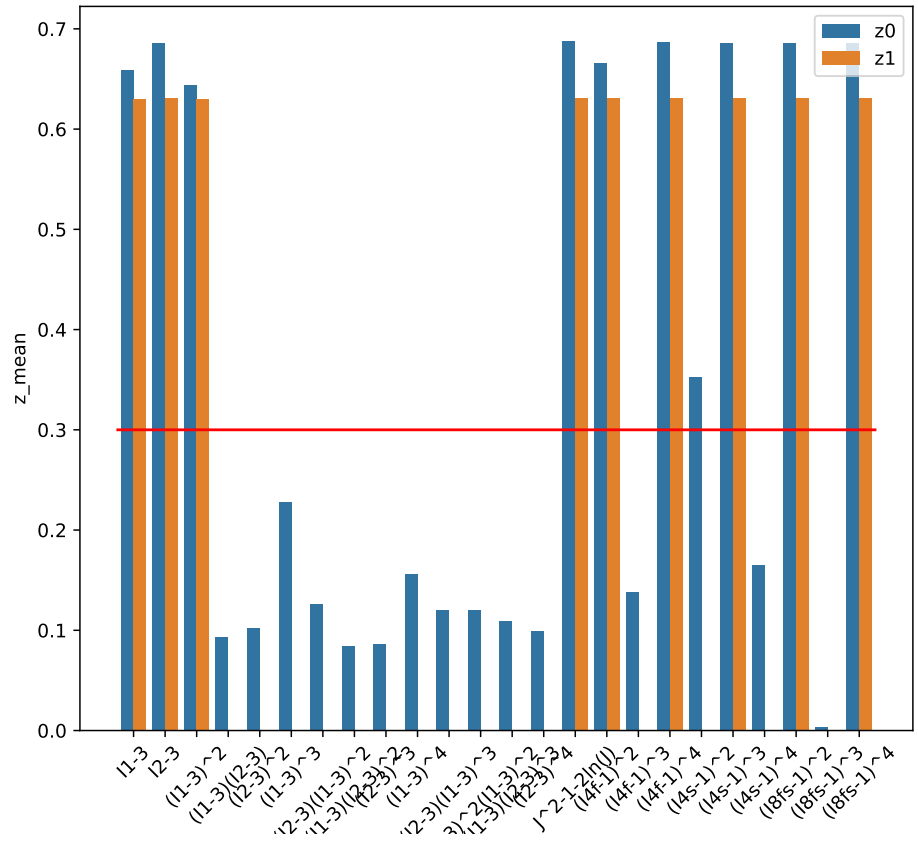

Fig. 36. The average z activity for all the features when considering the full deformation field, the most informative slice, and a uniaxially stretched sample.

Also in the Z-activity plot it is noticeable that the method has not yet converged, as the average -activity in the second iteration is only slightly higher than 0.6, which implies that roughly 60% of the sampled models use these features.
What is promising from these results, is that an orthotropic model can be obtained from uniaxial stretch tests alone. Further investigation might show good predictive results for models obtained from this training sample. In this case, even a simple uniaxial stretch test might be able to characterize the myocardium.